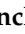





Review

# A Comprehensive Review on Current Performance, Challenges and Progress in Thin-Film Solar Cells

Santhosh Sivaraj<sup>1</sup>, Rajasekar Rathanasamy<sup>2</sup>, Gobinath Velu Kaliyannan<sup>3</sup>, Hitesh Panchal<sup>4,\*</sup>, Ali Jawad Alrubaie<sup>5</sup>, Mustafa Musa Jaber<sup>6</sup>, Zafar Said<sup>7,8,9,\*</sup> and Saim Memon<sup>10,\*</sup>

- <sup>1</sup> Department of Robotics and Automation, Easwari Engineering College, Ramapuram, Chennai 600089, Tamil Nadu, India
- <sup>2</sup> Department of Mechanical Engineering, Kongu Engineering College, Perundurai, Erode 638060, Tamil Nadu, India
- <sup>3</sup> Department of Mechatronics Engineering, Kongu Engineering College, Perundurai, Erode 638060, Tamil Nadu, India
- <sup>4</sup> Department of Mechanical Engineering, Government Engineering College, Patan 384265, Gujarat, India
- <sup>5</sup> Department of Medical Instrumentation Techniques Engineering, Al-Mustaqbal University College, Hilla 51001, Iraq
- <sup>6</sup> Department of Medical Instruments Engineering Techniques, Dijlah University College, Baghdad 10021, Iraq
- <sup>7</sup> Department of Sustainable and Renewable Energy Engineering, University of Sharjah, Sharjah P.O. Box 27272, United Arab Emirates
- <sup>8</sup> Department of Industrial and Mechanical Engineering, Lebanese American University (LAU), Byblos P.O. Box 36/S-122, Lebanon
- <sup>9</sup> U.S.-Pakistan Center for Advanced Studies in Energy (USPCAS-E), National University of Sciences and Technology (NUST), Islamabad 44000, Pakistan
- <sup>10</sup> School of Engineering, Arden University, Arden House, Middlemarch Park, Coventry CV34FJ, UK
- \* Correspondence: engineerhitesh2000@gmail.com (H.P.); zsaid@sharjah.ac.ae (Z.S.); smemon@arden.ac.uk (S.M.); Tel.: +44-(0)-2477297091 (S.M.)



**Citation:** Sivaraj, S.; Rathanasamy, R.; Kaliyannan, G.V.; Panchal, H.; Jawad Alrubaie, A.; Musa Jaber, M.; Said, Z.; Memon, S. A Comprehensive Review on Current Performance, Challenges and Progress in Thin-Film Solar Cells. *Energies* **2022**, *15*, 8688. <https://doi.org/10.3390/en15228688>

Academic Editor: Philippe Leclère

Received: 29 September 2022

Accepted: 14 November 2022

Published: 19 November 2022

**Publisher's Note:** MDPI stays neutral with regard to jurisdictional claims in published maps and institutional affiliations.



**Copyright:** © 2022 by the authors. Licensee MDPI, Basel, Switzerland. This article is an open access article distributed under the terms and conditions of the Creative Commons Attribution (CC BY) license (<https://creativecommons.org/licenses/by/4.0/>).

**Abstract:** Due to the recent surge in silicon demand for solar modules, thin-film photovoltaic (PV) modules have a potential to penetrate the market in significant numbers. As an alternate candidate, thin film technologies in PVs have the ability to achieve better performance. The competing thin-film PV technologies have the flexibility to adapt to any sort of curvature compared to rigid solar cells (SCs). Due to the peculiar characteristics of newer solar materials, stability issues, reflection losses, advancements in electrode materials and dopant materials with a photoactive layer are current challenges driving the industrial-academic voyage of development of solar materials for the betterment of Photo-conversion Efficiency (PCE). Based on the photoactive materials used over time, SC evolution was broadly classified into first, second and third generation SCs. In this review, the basic working mechanisms, various materials used, drawbacks and stability issues of different SCs are discussed extensively. Thin film SCs tend to absorb certain elastic deformations due to their flexible nature and to a certain extent. According to the NREL efficiency chart, multi-junctional SCs exhibit enhanced efficiency as compared to the other SCs. Among the third-generation SCs, the perovskite/Si tandem architecture shows a maximum efficiency of approximately 29%. Thin film flexible SCs find application in various sectors such as automobile, defense and/or energy storage devices

**Keywords:** solar cells; photo-absorber materials; working mechanism; thin film solar cells

## 1. Introduction

Solar energy is abundant, green and pure in the natural world and thermal and electrical energy may be produced efficiently using solar irradiance [1]. Electrical energy generated through sunlight follows the principle of the photoelectric effect [2]. According to this principle, an electron-hole pair is generated whenever higher energy photons impinge on the photoactive material [3]. This in turn is connected through an external circuit to

effectively employ the generated electrons. SCs are PV devices which make use of sunlight and convert it into useful electrical energy [4]. In contrast to fossil fuels, the electrical energy produced from post-manufactured PV devices do not emit CO<sub>2</sub>. As a result, solar-powered electricity has minimum impact on the environment. However, conventional energy sources cause the greenhouse effect, global warming, melting of polar ice bergs, gradual rise in sea level, and so on. One of the biggest difficulties with fossil fuels is that their prices are rising at an alarming rate, which brings an opportunity for the speeding up of various cutting edge PV technologies suitable for various industries and consumers [5]. Hence solar energy is perfectly suited to replace conventional fossil fuels in the near future. Irrespective of solar cells, the refractive index of their different layers plays a vital role in transmission of photons into the depletion region [6]. In addition, the surface reflection of incident light can be minimized through antireflective thin film coatings [7]. The selection of antireflective coatings should be based on a refractive index greater than that of the materials involved in interfacial layers of SCs. The reflected photons from the SC surface can be decreased through stronger antireflective films [8]. The coating thickness of antireflective films is also determined by the refractive indices of coating material and substrate material. The following flowchart represents the classification of SCs based on various factors.

As shown in Figure 1, SCs are typically classified by the rigidity of the solar material, i.e., rigid and flexible SCs. At an earlier stage, SCs were developed over rigid substrates, which has several disadvantages such as being somewhat heavier in weight, being difficult to install over any curvatures, and having a higher production cost [9]. However, rigid Silicon (Si) based SCs possess excellent stability, whilst. flexible thin film SCs are lesser in weight, can be installed over convenient curvatures, can be folded or rolled easily and fabrication cost is less. Stability is a major concern in flexible SCs. Based on the photo-active materials used at various stages, they are classified into first, second and third generation SCs. SCs are also categorized into homojunction and heterojunction SCs depending upon the number of materials that make up the photo-active layer [10]. Among all SCs, bulk heterojunction hybrid tandem SCs show the maximum PCE. Tandem SCs were developed for overcoming the drawbacks occurring in single material SCs such as the utilization of excess energy of incident light and easier transmission of low energy photons, without participation in the energy conversion process. Some of the commonly observed tandem architectures are two-terminal, mechanically ordered four-terminal and optically coupling four-terminal. With the help of a two-terminal tandem configuration, easier integration with the PV module was achieved than in single junction SCs. In mechanically ordered -terminal SCs, the sub-cells work with their own terminals leading to the non-requirement of the current-matching phenomenon [11]. Meanwhile, optically coupled tandem architecture was not integrated physically, but the sub-cells were coupled through an optical splitter positioned in an appropriate manner. Integration of sub-cells was more flexible with optically coupled tandem architecture, but costlier due to the inclusion of spectral filters [12]. In addition to capability in absorbing light which occurs at lower and higher wavelengths, the performance of tandem SCs can further improve through doping of impurities [2]. Because of the addition of impurities, there is a possibility of tuning the energy band gap of the photo-active layer [13]. As rigid SCs have been significantly engineered and have captured the entire solar market, we directly review thin film SCs and emerging thin film SCs from various perspectives. Figure 2 depicts the many generations of SCs as a flowchart.

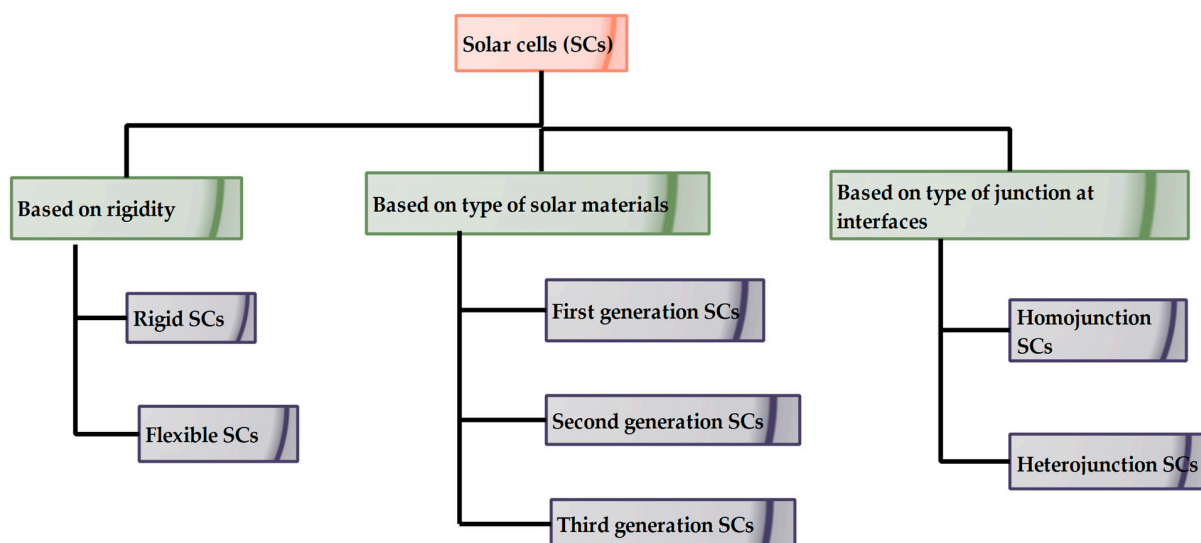


Figure 1. Classification of SCs based on various factors [9].

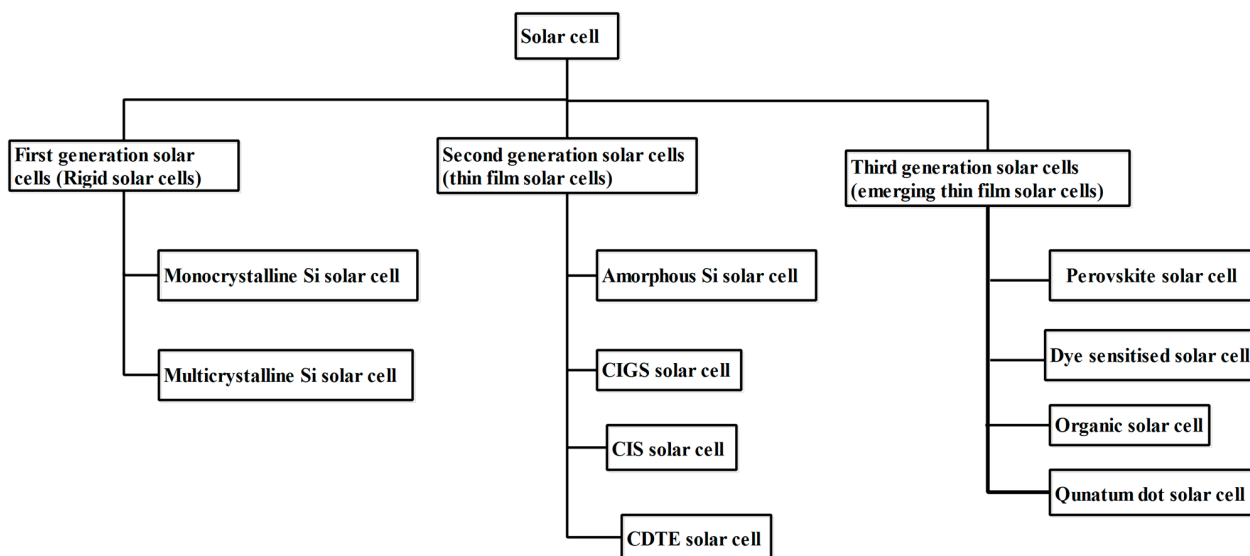


Figure 2. Classification of SCs based on photo-absorber materials.

## 2. Second Generation Solar Cells

### 2.1. Amorphous Silicon Solar Cells

As a non-crystalline direct band-gap semiconducting material, amorphous Si is utilized as a photo-absorber, in the form of light emitting diodes. Amorphous silicon (a-Si) is a non-crystalline form of silicon used for SCs as thin film transistors, used in LED displays. Due to a direct band gap, the incident light becomes absorbed with fewer micrometers of wavelength than for crystalline Si SCs [14]. For amorphous Si SCs, the tetrahedrally bonded Si atoms are arranged in a disordered fashion [15].

Due to the disordered nature of the materials, some atoms have dangling bonds. These dangling bonds are considered as defects in the structure of a-Si. The material can be passivated by the hydrogen atoms which bond with the dangling bonds and hence reduces their density. Hydrogenated a-Si (a-Si:H) possess sufficiently less defects and were mostly used in the field of PVs. a-Si:H was initially fabricated in the year 1969 by Chittick, Alexander and Sterling [16]. The major benefits of hydrogenation of a-Si are much easier fabrication and a much shorter energy payback period. However, hydrogenation leads to the material's light-induced degradation due to the Staebler-Wronski effect. Hydrogenation

also facilitates the possibility of doping in the a-Si:H SC. Furthermore, adding carbon atoms to the a-Si:H might improve the cell's electrical properties. This addition will lead to the improved transparency of the cell, which results in intensified light trapping and enhanced PCE [17]. The addition of carbon might also widen the band gap of a-Si:H. The increasing carbon content influences electron mobility, resulting in enhanced disorder in the elemental arrangement. More light can be transmitted into the depletion region of a-Si:H through utilizing TiO<sub>2</sub> nanosphere electrodes which were further coated with ITO in front contact [18].

The a-Si<sub>x</sub>Ge<sub>1-x</sub>:H based solar cell is a modified version of the hydrogenated amorphous Si SCs. This type of SC was prone to photosensitivity, with lesser energy band gap. A major drop in performance of a-Si:H due to the Staebler-Wronski effect was rectified through effective utilization of low band gap material [19]. By changing the composition of Si and Ge, the energy band gap of SC can be varied from 1.6 eV to 1.1 eV. Hence, absorption of light with longer wavelength was achieved [20]. Performance further improved through employing back reflectors made of Ag, Au, Al, etc. [21]

The p-n junction is not enough for efficient charge carrier collection because of the restricted hole mobility, to a certain extent, and of the higher defect density. Hence, an intrinsic absorber layer was introduced between the p- and n- region for charge carrier mobility. The order of arrangement of a-Si:H cell architecture may start with n-type or p-type material. Based on the deposition sequence, there are two possible architectures for a-Si:H cell: superstrate or PiN configuration, and Substrate or NIP configuration [22,23]. The schematic diagrams in Figures 3 and 4 represent the simple architecture of a-Si SC in superstrate and substrate configuration.



**Figure 3.** Superstrate configuration.

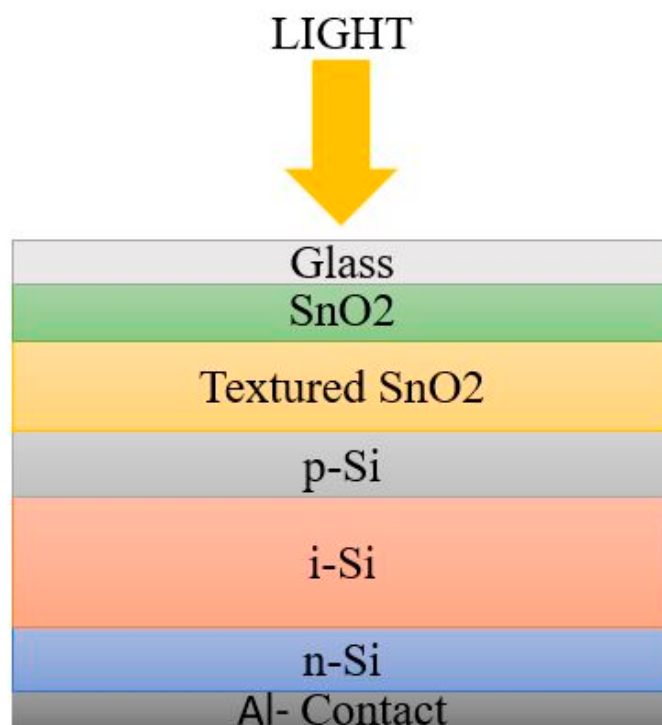


**Figure 4.** Substrate configuration.

For effective exciton generation and hole collection, the cell is designed in such a way that the light incidence occurs initially only with the p-type material. Typically, the a-Si:H cell architecture consists of TCO, p-type a-Si:H, an intrinsic a-Si:H absorber layer, n-type a-Si:H and metal contact [23]. In order to obtain better electrical contact for SC, TCO must be the front contact while the back contact may be either conductive metal or TCO. The open circuit voltage was enhanced by a wider bandgap for the active intrinsic absorber layer [24]. Some foreign elements such as oxygen, carbon, etc., when reinforced with the a-Si:H might also widen the bandgap. The superstrate and substrate were also differentiated by means of transmissivity behavior. The superstrate configuration is most probably temperature resistant and transparent in nature, hence all PIN configurations were preferred for the fabrication of solar modules [25], but the substrate configuration is opaque in nature and preferred for flexible SCs. There are various thin film-based silicon materials such as nanocrystalline silicon, proto-crystalline silicon and polymorphous silicon. The nanocrystalline silicon ( $\mu\text{c-Si:H}$ ) has a narrow bandgap material as compared to wider band gap a-Si:H material. Here, the crystallite size varies from a few micro- to nano-meters. The continual nucleation phase of  $\mu\text{c-Si:H}$  possesses an undeveloped crystallite structure, known as proto-crystalline silicon (pc-Si:H) [26]. These are formed by the hydrogen dilution of  $\text{SiH}_4$ , which is much closer to the interfacial phase of a-Si:H to  $\mu\text{c-Si:H}$ . Some of the major advantages of pc-Si:H are wider bandgap material and less density. Soon after, the attainment of critical thickness layers always seemed to consist of a microcrystalline structure [27]. If the silicon is grown in the plasma phase in the intermediate structural appearance, between the a-Si:H and  $\mu\text{c-Si:H}$ , then it is known as polymorphous silicon (pm-Si:H) [28]. During the deposition process, pm-Si:H was deposited over the entire layer depth with uniform homogeneity. Among all other silicon based structures, light induced degradation gives a faster rate for pm-Si:H. Defects of a-Si:H are band-tail state defects and mid-gap defect states [29]. Doping of foreign elements into the a-Si:H absorber layer might result in a change of fermi level. The heterojunction architecture might also utilize the fraction of unabsorbed incident light, in addition to the absorbed light, for the betterment of PCE in a-Si:H based SC. In a single junction SC, the chance of light absorption is at a particular wavelength, but in a multijunction SC, the cell has a capability to absorb light

at varied energy levels [30]. Figure 5 represents the a-Si:H&a-SiGe:H heterojunction SC, which is capable of converting more photons into electrical energy.

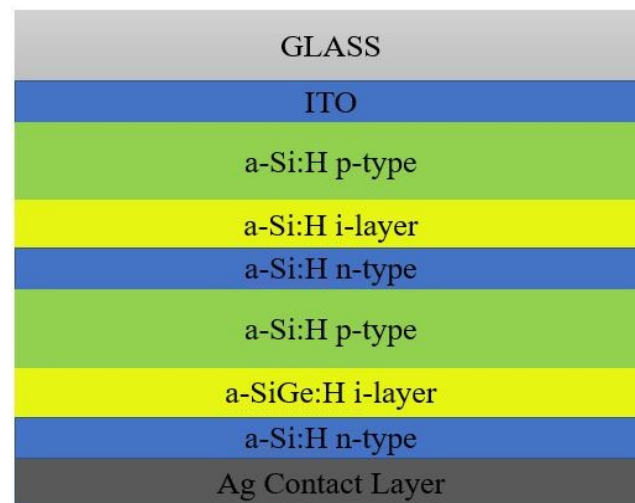


**Figure 5.** a-Si:H&a-SiGe:H heterojunction SC.

Mid-gap defect states possess sites of effective recombination centers, a major threat to all electronic devices [31]. Band tail states have been described as some of the energy states which are constrained to a particular extent, but only in between the valence and conduction band. Table 1 represents a comparison of the various a-Si cells, developed with various materials, along with their output parameters. This is a distribution of Urbach energy exponentially. Some of the advantages of a-Si:H over C-Si are [32]

- Simple working mechanism and inexpensive
- With optimal thickness, light absorption is higher than in the C-Si
- Lesser raw material is required
- The capability to adhere over any sort of surfaces.

In addition to these advantages, some of the disadvantages of Si:H SCs are as follows

- Lesser working life due to low hole-mobility
- Harmful gases were needed during fabrication process [33]
- Mostly absorbs light at a wavelength not greater than 700 nm.

**Table 1.** Comparison of PV performance of various a-Si:H based SCs.

S.No	Absorber Material	Voc (V)	Jsc (mA/cm <sup>2</sup> )	FF	eff	Ref
1	μc-Si:H	0.542	27.44	73.8	10.97	[31]
2	μc-Si:H	1.411	12.6	67.8	12.1	[34]
3	a-Si n type	0.704	42.4	82.6	24.7	[35]
4	a-Si:H	0.877	17.28	66.6	10.09	[36]
5	μc-Si:H	0.548	29.39	73.1	11.77	[37]
6	a-Si:H	0.896	16.36	69.8	10.22	[37]
7	μc-Si:H	1.322	13.02	69	11.9	[38]
8	a-Si:H μc-Si:H μc-Si:H	1.936	8.96	71.5	12.41	[39]
9	μc-Si:H	0.521	28.17	71.6	10.5	[40]
10	a-Si:H μc-Si:H μc-Si:H	1.901	9.92	72.1	13.46	[41]



## 2.2. CIGS Solar Cell

Because of its higher absorption coefficient, CIGS was employed as primary absorber material with generalized structure as  $\text{CuIn}_{(1-x)}\text{Ga}_x\text{Se}_2$ , similarly to the CdTe architecture. The energy bandgap can be altered by modifying Cd and Ga composition [42]. The junction behavior of CdS and CIGS with respect to the defects does not cause any major change to the device performance [43]. The following mathematical equation (1) gives the bandgap of the CIGS with an active material structure  $\text{Cu In}_{(1-x)}\text{Ga}_x\text{Se}_2$ .

$$E_g = 1.01 + 0.626x - 0.167x(1 - x) \text{ eV} \quad (1)$$

For example, if the value of  $x$  is 0.1 which might be the composition of Ga, then the energy bandgap was approximated as 1.058 eV. The band gap significantly changes in accordance with the doping level of Ga. In case of CIS, the band gap can be estimated by substituting the value of  $x$  as 0, hence the band gap will be 1.01 eV. So, for commercial CIGS, the bandgap varies between 1.01 to 1.1 eV. Their melting point was 985 °C. Generally, CIGS is a p-type material and CdS is a n-type material, which combine together to obtain a p-n junction. In such devices, there is the existence of selenium, which influences the electrical properties of the material [44]. The presence of four elements makes the fabrication process more challenging.

The CdS in the CIGS SC can be deposited through chemical bath deposition. It can be synthesized with the use of salts such as  $\text{CdSO}_4$ ,  $\text{CdCl}_2$ ,  $\text{CdI}_2$ , etc., of an aqueous nature. In addition to this complexing agent,  $\text{NH}_3$  and thiourea were stirred and heated to optimal temperature and concentration to obtain the CdS material. CdS should be grown in a pseudo-epitaxial manner and seems to be an intermediate structure between polycrystalline and single crystalline structures. At the interface of CdS and CIGS, there is an option of accommodation of the foreign material CdSe, which hinders the cell's performance. With proper design under optimal conditions, CdSe accumulation can be avoided. In this device, there are also transparent conducting electrodes such as  $\text{InSnO}$ ,  $\text{SnO}_2$ , which were synthesized through sputtering, evaporation or by atomic layer chemical vapor deposition [45,46]. On top of this layer, there is a buffer layer which is probably ZnO, possessing higher resistivity. This in turn reduces the defect intensity at the interfaces and improves the diode quality. It also increases the shunt resistance; hence, the leakage has been reduced. The top contact will be the metal contact with an aluminum grid on top. The various possible fabrication techniques of CIGS SC are evaporation, sputtering, closed space sublimation, spray pyrolysis, chemical bath deposition and the two-step process: metal deposition followed by salinization [47]. A cross sectional diagram of the CIGS SC, whose cell architecture is glass substrate/Mo/p-type CIGS/n-type CdS/i- ZnO/Zno:Al/MgF<sub>2</sub> ARC/Metal grid, is depicted in Figure 6. In case of substrate configuration, the light enters through TCO, and over the substrate the back contact material is deposited. For the superstrate configuration, incident light enters through the glass surface and that performs as a window for the photocurrent generation process.

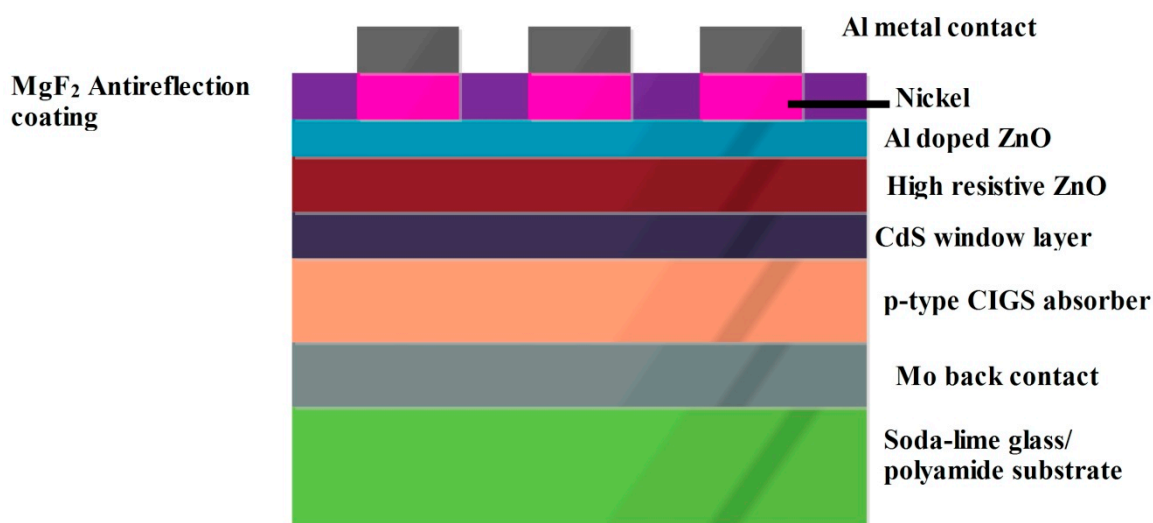


**Figure 6.** Diagrammatic representation of CIGS cell architecture.

CIGS SCs can be used in place of conventional Si solar cells. In flexible CIGS SCs, which are a multilayered device, a crucial performance inhibitor was interfacial layers, which need to be selected based on stability against mechanical stress, resistance towards temperature and thermal expansion coefficient [48]. In general, Mo was used as back contact for flexible as well as rigid CIGS SCs. In the case of flexible solar cells, Mo with bigger grains are prone to exert internal minor cracks during plastic deformation of flexible SCs. The thickness of buffer layer CdS also plays a major role in performance of the solar cell. An increase in thickness of the CdS layer facilitates absorption of more photons of shorter wavelength. This leads to a smaller quantity photons reaching the depletion region and is also involved in the power conversion process. In addition to this, the charge carrier mobility of the CdS buffer layer was low compared to the CIGS absorber layer, which also degrades the current conversion efficiency of CIGS SC. Hence, the thickness of buffer layer CdS should be kept as low as possible for the attainment of elevated cell performance [49].

After the light incidence, the CdS layer of an energy bandgap greater than 2.4 eV allows the photons to reach the absorber layer. The exciton is generated in the active layer. Because of the built-in electric field across the interfaces of p- and n- type material, the generated electrons diffuse into the n-type material and, further, reach the n-electrode, while the generated holes diffuse into the p-type material and then collect at the p-electrode. The back surface field created near the Mo back contact layer helps the escaped electrons to be redirected towards the p-n junction, then reach the n-electrode. Si SC is predominantly used all over the world at present, due to its eases of use and abundant availability compared to other raw materials. Many other alternatives are currently under as effective replacements for Si SC [50]. CIGS are engineered and used in place of Si SC. They are less prone to mechanical damage compared to Si SCs. The losses incurred with J<sub>sc</sub> were rectified by the use of different layers. Monolithic integration during fabrication is not possible with Si SC, but is possible with the CIGS.

Si is an indirect bandgap semiconductor and its absorption coefficient is rather low ( $10^4 \text{ cm}^{-1}$ ), while CIGS is a direct band gap semiconductor with much higher absorption coefficient. For this reason, CIGS can be fabricated with a thickness as much as 100 times that of Si SC [51]. The CIGS cell architecture is much similar than that of the tandem SCs, where the high energy photons are absorbed by the CdS layer, while the photons with less energy are simply transmitted to the active layer. There, these latter photons are absorbed, resulting in better utilization of the incident photons. Exciton recombination occurs at the interface of the window buffer layer and the active layer, mainly due to the conduction band discontinuity. The level of discontinuity directly affects the energy bandgap, which increases in accordance with the increase in the discontinuity [52]. Thin-film flexible SC



opens up a new field in the SC market. Flexible substrates are easy to adopt any sort of curvature, lighter in weight and rolled easily. Their production cost is also less and they are likely to be fabricated through Roll-to-Roll manufacturing. Polyimide substrates have been used for flexible CIGS SCs [53]. There are three different substrates used in CIGS SCs: polymer sheets, ceramics and metallic foils. A higher efficiency of CIGS has been reported with the usage of polyimide substrates

Regarding the chemical composition of CIGS, it is clear that they are a quaternary compound. Uniform constitution of elements over the entire surface of the SC results in optimal photocurrent generation, but attaining uniformity over larger areas is very difficult. For SCs of larger area, PCE is generally low. For large area substrates, sputter coating is most suitable for obtaining uniformity in distribution [54]. Thickness of the deposited layers and chemical composition can be examined through optical characterization techniques. Coming to the commercialization of long range CIGS, there is a conflict between the size increment and the PCE. These factors cannot be compromised. Cds possess higher toxicity and are harmful to the surrounding environment. As they are toxic, their proper disposal is arduous [55]. Hence, Cd free CIGS solar panels have been focused on instead. Indium is the key element which is responsible for the price of CIGS panels. The main source of Indium is as a by-product of Zn production. This can be overcome through a preference for flexible, thin, solar CIGS in place of rigid CIGS. without disturbing the PV parameter/ $J_{sc}$ . In addition to this, the time taken to process TCO and CIGS layers seems to be much higher. This should be reduced by adopting a thin CIGS layer and quicker growth techniques [56]. Table 2 represents a comparison of the various CIGS cells developed with various architectures, along with their output parameters.

Some of the major advantages and disadvantages of CIGS SCs are as follows:

- They are more resistant to heat than Si SCs.
- The active material (CIGS) does not contain harmful components.
- Holds easily tunable bandgap, facilitating tandem architecture.
- Its grain boundaries acts as buffer layer, which inhibits the surface recombination.

Some of the disadvantages of CIGS SCs are:

- Achieving improved performance takes longer than Si SCs.
- Less efficient than conventional SCs.

**Table 2.** Comparisons of PV performance of various CIGS based SCs.

S.No	Cell Architecture	Inference	Voc (V)	Jsc (mA cm <sup>-2</sup> )	FF (%)	Eff (%)	Ref
1.		Mo-N back contact diffusion barrier deposition in CIGS SC	0.622	28.67	67.53	12.05	[57]
2.		alkali post deposition treatment of RbF	0.741	37.8	80.6	22.66	[58]
3.	glass/Mo/CIGS/CdS/i-ZnO/TCO/Au	CdS buffer layer deposition through chemical bath method, effect of i-ZnO high resistive layer	0.661	32.08	78.9	15.50	[59]
4.		high mobility TCO with 1 eV absorbers	0.609	42.3	74.6	19.20	[60]
5.	Mo/Si/CIGS/ZnS/ZnO	impact of silicon inclusion to reduce the cell thickness and influence of thickness and gallium concentration of the CIGS absorber layer on the performance	0.6903	37.57	81.03	21.08	[61]
6.	ZnO NWs/AZO/ZnS/CIGS/Mo/Thermal electric generator	enhanced performance achieved by ZnO NWs with CIGS SC along with series connection of Thermal electric generator	0.85	38.55	67.2	22.02	[62]
7.	(Ni/Al)/MgF <sub>2</sub> /Al:ZnO/CdS/(KF-PDT/CIGS)/Mo/SLG	influence of light-soaking, heat-soaking, and combined LS and HS on KF-treated and KF-free CIGS SCs with CBD-CdS buffer layer					[63]
8.	ZnO/Buffer n-ZnS/p-CIGS/Mo	effect of ZnS buffer layer	0.804	35.66	82.14	23.54	[64]
9.	Al <sub>2</sub> O <sub>3</sub> /MgF <sub>2</sub> /AZO/i-ZnO/CdS/CIGS/Mo	effect of thickness of ARC over CIGS cell		31.22			[65]
10.	(Al/Ni)/TCO/CdS/GaO <sub>x</sub> /CIGS/Mo/Soda-lime glass	gallium oxide deposited by plasma-enhanced atomic layer deposition, as a surface passivation material at the interface of CdS buffer layer of CIGS SC	0.056	1	8.22	2.60	[66]
11.	(glass/stainless steel)/Mo/CIGS/CdS/ZnO NWs/ITO	ZnO NWS incorporated in CIGS and the effect of externally applied stress (rigid) and strain (flexible)				11.40 (stress) 5.96 (strain)	[67]

### 2.3. CdTe Solar Cell

Cubic tetrahedral crystalline natured CdTe contains Cd and Te with two and six valence electrons and a band gap of 1.44 eV. The obtained band gap is below mono-junction SC's limiting optical band gap range [68]. Inclusion of Selenium with the CdTe was also a reason for better performance of this cell [69]. This was performed by an interdiffusion process with the use of a CdSe precursor, especially at the elevated temperatures of CdTe deposition [70]. However, selenium, including CdTe via diffusion, find it difficult to absorb light of longer wavelength. Hence CdSe<sub>x</sub>Te<sub>1-x</sub> synthesized through close space sublimation of about 600 nm thickness increases the ability of long wavelength light absorption, which also results in enhanced PCE. The substrate temperature of CdS deposition has a direct effect on the crystal structure. As the temperature increases, the grain size and crystallinity increases, then interdiffusion is easier for the various layers of semiconductor. Figure 7 represents the simple cell architecture of the CdTe SC [71]. The band gap of CdTe is 1.5 eV, which was within the range of photo-absorber material for generating the photocurrent from incident light [72]. A theoretical efficiency of about 30% was not achieved practically (10–15%) due to various factors, such as the short lifetime of the charge carrier, higher opaqueness of window layer and TCO glass, less stability of doped CdTe films and poor ohmic contact within the interfacial layers of CdTe SC [73].

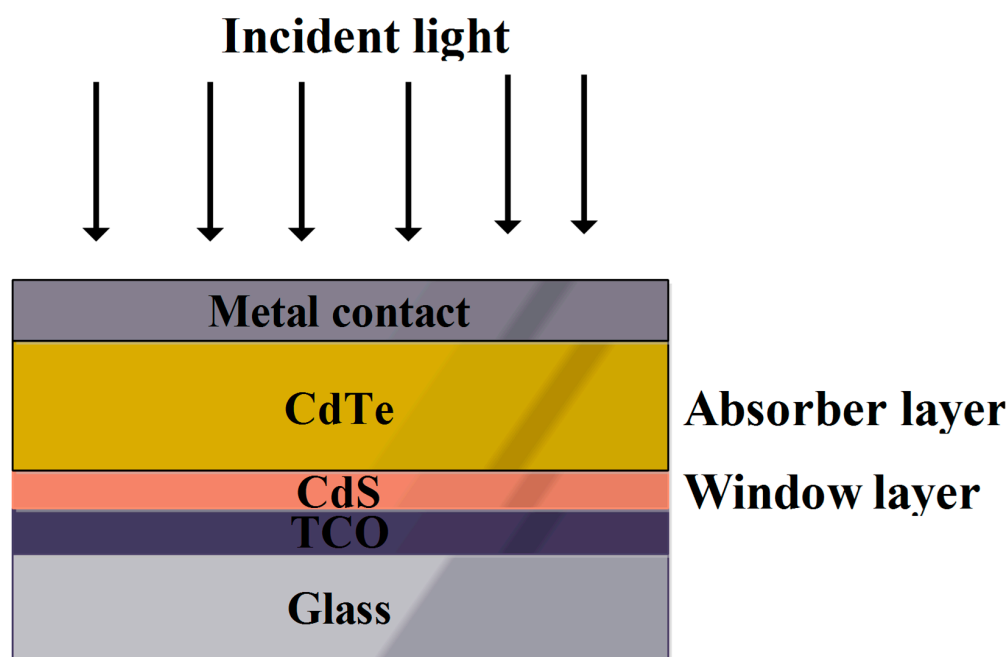


**Figure 7.** Pictorial representation of simple CdTe SC [74].

In CdTe SCs, conductive, stable and transparent natured TCO was preferred. However, using TCO as front contact of the cell architecture leads to the superstrate configuration as illustrated in Figure 7 [74]. The most commonly used materials as TCO were Al doped ZnO(ZnO:Al) and SnO<sub>2</sub>:In<sub>2</sub>O<sub>3</sub> (ITO) in CdTeSCs. The major advantage of these materials are much higher transparency and lower electrical resistance [74]. The main drawback of ZnO:Al as TCO is that they tend to breakdown easily at temperatures greater than 400 °C. The ITO at higher temperatures also makes the indium diffuse into the CdTe layer. However, the most suitable material at higher process temperatures greater than 500 °C is SnO<sub>2</sub>:F, which is commonly known as FTO. Other than these materials, the most suitable alternative, especially for CdTe, is Cd<sub>2</sub>SnO<sub>4</sub> [75].

The CdS is most likely to be used as a window layer in CdTe SCs. The window layer's main function is collecting the generated excitons from the CdTe active layer. The window layer does not absorb incident light of wavelengths less than 520 nm. Hence there is a degradation in overall performance. The solution for this problem is reducing the thickness

of the window layer [76]. The thickness should not be less than 100 nm, as this might lead to substantial losses in Voc and fill factor. Furthermore, reduction of thickness might create voids in the microstructure of CdS, which also degrades the cell performance. This can be avoided by the implementation of buffer layer between the CdS and CdTe materials. The CdS layer is generally a n-type material and can be deposited through the following techniques: chemical bath deposition, RF sputtering, close space sublimation and thermal evaporation. The oxidized CdS layer presents an increased energy band gap than the actual CdS layer, hence light absorption is further increased. In recent research, an alternative material for CdS is  $Mg_{1-x}Zn_xO$  (MZO) [77].

CdTe is a thin film active material which is usually polycrystalline in nature. The PV performance of the absorber layer is usually based on the techniques with which the absorber layer was deposited [78]. Some of the techniques preferred for the deposition of the active layer are RF sputtering, electrodeposition, thermal evaporation, close space sublimation, etc., and among these, close space sublimation is highly preferred. The major drawback of CdTe is that they hold lower carrier lifetime. Due to the presence of dangling bonds, the interstitial spacing between the grains will act as the active site for the exciton recombination. With the use of characterization techniques such as electron back-scattered diffraction, the level of orientation of grain boundaries, crystalline nature of the deposited film, etc., can be examined [79].

The design and implementation of back contact in CdTe SC is rather challenging. CdTe is a material with higher ionization potential. Hence, its work function is greater than 5.2 eV for ohmic contact. Lower work function materials lead to the creation of a Schottky junction especially at the interface of CdTe and the metal surface [80]. Some of the materials whose work function is nearer to the above specified are Ni and Pt, but they readily react with the telluride, hence they remain unusable. Some of the materials with higher dopant densities and better stability are ZnTe, Al doped Te,  $FeS_2$ , NiP, etc., capable of forming ohmic contacts. These materials with better ohmic contact can increase the working life of a module by up to 20 years [81].

CdTe is generally stable in nature. However, some problems were encountered, such as degradation due to improper encapsulation in the cell architecture. Diffusion of copper into the cell architecture also reduces cell performance, which can be overcome through reducing the copper content with the addition of a barrier layer of Zinc Telluride,  $As_2Te_3$  [82]. In the case of CdTe solar modules, there is no issue with the photo-stability, while in the case of a flexible CdTe cell, more factors affect the stability of the cell. The problem is due mainly to the thin films' bending, tension and compression. This literature studied the effect of compressive and tensile stresses experienced by thin films installed over different architectures. Thus, efficiencies were not dependent on the substrates, but on stresses (9). CdTe with different substrates has also been studied for the effect of stresses. It is found that the thin film's polyimide exhibits more incremental distortion than the rigid glass substrate. Polyimide substrates were also easily affected by UV-irradiation, which can be overcome through anti-UV coatings. Table 3 gives the comparison of various CdS SCs, along with their cell architectures. Some of the major advantages and disadvantages of CdTeSCs are as follows:

- The preparation of CdTe SCs was performed in minimal time duration, compared to other SCs.
- It has a direct band gap with energy of 1.4 eV.
- It can absorb much shorter wavelengths than silicon solar panels.
- Raw material Cd was obtained as a sub-product of zinc extraction, hence has less price fluctuation than Si.

**Table 3.** Comparison of various CdS SCs along with their cell architectures.

S.no	Cell Architecture	Voc (mV)	Jsc (mAcm <sup>-2</sup> )	FF	η (%)	Ref.
1.	Glass/FTO/n-CdS/n-CdTe/p-CdTe/Au	730	33.8	0.62	15.30	[83]
2.	Glass/FTO/CdS/CdTe	838	25	0.72	15.20	[84]
3.	glass/FTO/CdS/CdSe/CdTe/ZnTe:Cu/Au	791	27.4		13.47	[85]
4.		861	26.9	0.754	17.50	[71]
5.		863	28.6	0.781	19.25	[86]
6.	Glass/ZnO:Al/n-CdS/p-CdTe/ZnTe	1528.5	28.355	0.497	21.57	[87]
7.	Glass/n-FTO/n-Cd(S,O)/p-CdTe/p-CuZnTe/Au	848	26.6	0.733	16.60	[88]
8.	ZnO/CdS/CdTe (0.25/0.05/2.5 micrometers)	859	28.4	0.737	17.66	[89]
9.	Quartz/Ti/SiO <sub>2</sub> /CdTe/IITO		40.36			[90]
10.	Sodalime glass/SnO <sub>2</sub> :F/SnO <sub>2</sub> /CdS:O/CdTe/(Cu/Au)	857	23.6	0.672	14.10	[91]
11.	SiO <sub>2</sub> /Si(DBR)/ZnTe (BSF)/CdTe/CdS/ZnO/FTO.	109,820	1201	0.8203	10.39	[92]
12.	glass/SnO <sub>2</sub> :F(FTO)/n-CdS/ p-CdTe/Cu/V <sub>2</sub> O <sub>5</sub> /Cu/Au	806	24.8	0.7	14	[84]

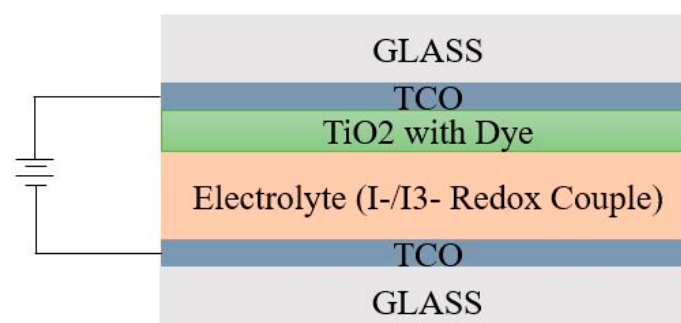
Some of the disadvantages of CdTe SCs are:

- Delivers less power output than Si SCs.
- Even though Cd was easily available, Te was rarely found in the crust.
- Cd was highly toxic and its disposal was a rather difficult process.

### 3. Third Generation Solar Cells

#### 3.1. Dye sensitised Solar Cells

Dye sensitized solar cell (DSSC) is a SC which mimics the photosynthesis process of plants leading to generation of photoelectrons [93]. DSSCs generally comprise photo-electrolyte, TCO electrode, TiO<sub>2</sub> electrode and encasing glass [94]. The electrolyte in DSSC should be stable, non-hazardous, solvent, with high ionic conductivity and better interaction with dye. Meanwhile, the counter electrode (metal or non-metal) should hold a higher surface area and high catalytic activity. Hence, platinum is the most commonly used counter electrode. Initially, light absorbed dye molecules become sensitized. The sensitized dye molecules in addition to the TiO<sub>2</sub> molecules lead to electron generation and oxidation of the sensitized dye. The schematic diagram Figure 8 represents the simple DSSC architecture [95]. Operation of DSSC varies with conventional semiconductor based SCs as absorption of incident light and exciton generation do not occur cordially as in conventional cells. In this cell, the light is initially incident over the cell surface. Over the glass surface, the electrode TCO was coated, via which the generated electrons were transferred to another electrode by means of an external circuit [96]. From the NREL efficiency chart, it is evident that a maximum power conversion efficiency of 13.0% was experienced by the DSSCs. Room temperature synthesis of DSSC is a major advantage, but maintaining stability and photodegradation was difficult [97].

**Figure 8.** Simple cell architecture of DSSC.

Due to technical advancements, instead of TCO, graphene has been used because of its better conductivity at very minimal thickness, and it also holds better transmittance. Both nano-fibred  $\text{TiO}_2$  and graphene can also be used as a photoanode. Redox reaction at the electrolyte significantly helps dye regeneration. This electron then enters into the counter electrode, which brings the  $\text{TiO}_2$  back to its original state. The electrons that flow back to the circuit react with the iodine ions [98]. Then the iodine ions are converted from one state to another; this, in turn, is responsible for conversion of the excited dye molecules to their original unexcited state. In this way, regeneration of dye occurs. The electron transfer between the counter electrodes leads to electricity generation. The electrode may be nanostructured  $\text{TiO}_2$ , or  $\text{ZnO}$  can be used. Optimization of photoelectrode thickness is extremely important through experimentation and simulation. The photosensitizer basically consisted of polypyridyl compounds of ruthenium or osmium. Anthocyanins, flavonoids, betalains, etc., are some of the dyes used in DSSC. The most commonly used electrolyte is  $\text{I}^-/\text{I}_3^-$  redox couple, while  $\text{NaI}$ ,  $\text{LiI}$  dissolved in non-protonic solvents such as acetonitrile, propylene carbonate, etc., are used as electrolytes. These electrolytes transform the excited dye to an unexcited state. For obtaining better PCE, the ionic conductivity of electrolyte must be higher [99]. Instead of liquid dye, the thin absorber material is used for light trapping; then such a cell is known as an extremely thin absorber SC.

The leakage of liquid electrolyte may be a major drawback in DSSCs, which is overcome through the use of quasi-solid state electrolytes [100]. The main advantage of this particular electrolyte is enhanced ionic conductivity with better mechanical strength. In place of the dye incorporated electrode, the perovskite infused electrode might give rise to the development of a new field of SC, i.e., Meso-structured SC. PCE is mainly affected by the nature of the excited and ground state photo-sensitisers, Fermi level of the photo-electrode and redox potential of the electrolyte [101]. In Table 4, various cell architecture materials of DSSC are compared with their output PV performance.

Some of the major advantages of the DSSC are as follows:

- Easier to fabricate under normal ambient condition.
- Lower fabrication cost.
- Better performance under higher working temperature and diffused light.

Major drawbacks of DSSC are and further distinguished in Table 4:

- Usage of liquid dye might leak which leads to defective SC.
- Platinum is used as a counter electrode in order to improve the dye regeneration, redox reaction and PCE, which was available only at higher cost when  $\text{TiO}_2$  was used.
- Ruthenium or osmium-based dye is versatile and not easily available at wider range; it is better to prefer dyes based on simple elements.
- The maximum PCE reported until now was 14.3%, which used a silyl linker with the triarylamine and cobalt redox couple.
- Degradation of electrolyte materials.
- Electrolytes possess a low freezing temperature, while at higher temperatures a sealing issues might arise. Solid state dyes were engineered to overcome the liquid state dyes' drawbacks [102].



**Table 4.** Various materials used as essential parts of DSSCs with their PV performance.

S.No	Dye Used	Electrode Used	Counter Electrode Used	Electrolytes Used	Max. PCE (%)	Max. Fill Factor	Voc (V)	Jsc (mA cm <sup>-2</sup> )	Ref.
1.	Chlorophyll pigments	TiO <sub>2</sub>	graphite			0.49	0.44		[103]
2.	Acanthus sennii chiovenda flower and Euphorbia cotinifolia leaf	TiO <sub>2</sub>	(PEDOT-coated FTO glass)	polymer gel electrolyte	0.15 & 0.136	0.47 to 0.6	0.475 to 0.507	0.352 to 0.642	[104]
3.	N-719 dye	TiO <sub>2</sub>	cobalt-nickel selenide nanoparticles dispersed on graphene nanosheets	I <sup>-</sup> /I <sub>3</sub> <sup>-</sup> redox electrolyte	9.42	0.683	0.75	18.33	[105]
4.	N-719 dye	TiO <sub>2</sub>	activated coconut shell charcoal	I <sup>-</sup> /I <sub>3</sub> <sup>-</sup> redox electrolyte	7.85	0.62	0.65	19.49	[106]
5.	Betalains and anthocyanins	TiO <sub>2</sub>	platinum metal clusters		2.06		0.316 to 0.419	8.8	[107]
6.			Co/Se and Ni/Se nanocomposite	I <sup>-</sup> /I <sub>3</sub> <sup>-</sup> redox electrolyte	6.43 & 5.23				[108]
7.	Rhoeo spathacea dye	TiO <sub>2</sub> adsorbed Au nanoparticles	Pt	aqueous electrolyte of Ce <sub>4</sub> <sup>+</sup> /Ce <sub>3</sub> <sup>+</sup> system.	1.49				[109]
8.	Anthocyanin dye	TiO <sub>2</sub>	conductive plastic sheets containing graphite						[110]
9.	N3 dye	nano sized Cu with carbon dispersed in TiO <sub>2</sub>		I <sup>-</sup> /I <sub>3</sub> <sup>-</sup> redox electrolyte	2.8 & 23	0.55–0.70	0.76 to 0.81	6.1–7.4	[111]
10.	20% Basella alba(green dye) and 80% Amaranthus dubius (Red dye)	TiO <sub>2</sub>	carbon coating		0.847	0.515	0.385		[112]
11.	Dye from Pawpaw Leaf and Flame Tree Flower mixture	TiO <sub>2</sub>	Pt		0.27	0.69	0.518	0.744	[113]
12.	C106 dye	double layered TiO <sub>2</sub>	Pt	Z988 electrolyte	9	0.762	0.694	8.702	[114]
13.	Male flowers Luffa cylindrica	TiO <sub>2</sub>	Pt		0.13	0.60,	0.52	0.44	[115]
14.	Spinach and ipomoea	TiO <sub>2</sub>	Pt		0.131& 0.278	0.51 & 0.563	0.5 & 0.54		[116]
15.	Bixin, annato, Norbixin from Achiote seeds	TiO <sub>2</sub> & ZnO <sub>2</sub>	Pt		0.37 (max)	0.59	0.57	1.1	[117]

### 3.2. Perovskite Solar Cells

Perovskite solar cells (PSC) with  $ABX_3$  architecture showed a faster rate in terms of PCE within a shorter period of time. On the other hand, A, B and X are often referred to as monovalent cation, divalent cation and monovalent anion. Perovskite material possesses better photophysical properties such as tunable band gap, high absorption coefficient, etc., [118]. Because of these properties, these materials find application not only in the field of SCs but also in LEDs, photo detectors and photodiodes [119]. Initially,  $BaTiO_3$  and  $CaTiO_3$  perovskites were mainly utilized for photodetectors due to their extensive ferroelectric properties. Various ferroelectric materials were fabricated with  $CaTiO_3$  or  $BaTiO_3$  as base material. With suitable substitution of the organic cation and changing of the crystal structure, perovskite with a tunable band gap were easily developed. Some of the superior properties of organic perovskite in comparison with the conventional inorganic perovskites are [120]:

- Higher PCE.
- Higher absorption coefficient.
- Fabrication can be carried out through solution processing technique and wafer-based approach.
- Diffusion length is higher with higher charge carrier mobilities.

Some of the drawbacks encountered in perovskite SCs are as follows:

- Poor encapsulation leads to the degradation of perovskite material.
- Lead based Perovskite material is toxic in nature.

Due to these properties, the generated electron might travel much more distance, generate current before recombining and avoid energy loss due to heat within the cell. In the case of single perovskite, the stoichiometry appears to be  $AMX_3$ . At the same time, X is oxide or halide anions and B refers to a metal cation with a coordination number of 6. A can be Ca, K, Na, Pb, Sr, etc. In a crystalline structure, M lies at the center of the cell, X occupies the facing center of the cell and A occupies the eight corner atoms. The measure of the degree of distortion in the crystal structure of perovskite in an ideal cubic form is represented in following Equation (2) [121].

$$t = \frac{(r_A + r_M)}{\sqrt{2} (r_M + r_X)} \quad (2)$$

where  $r_A$  is the radius of A cation,  $r_B$  is the radius of B cation and  $r_X$  is the radius of halide anions.

The tolerance factor for oxide-based perovskites and oxide halides ranges from  $0.89 < t < 1$  to  $0.85 < t < 1.11$ . The most commonly used perovskite material for obtaining high efficiency SC is methylammonium lead iodide.  $CH_3NH_3PbI_3$  is a semiconducting material with a direct band gap of about 1.55 electron volts, in addition to a higher absorption coefficient ranging from  $10^4$  to  $10^5 \text{ cm}^{-1}$  [122]. Various research has been carried out with this material and by also altering the B site and X site materials using materials with similar property [123]. Whenever sunlight occurs over the perovskite material, A site cations might migrate along the crystal structure. This phenomenon is known as ion migration, which leads to the poor photo-stability of the cell. Due to the ion migration, the 3D perovskite structure becomes converted into a 2D perovskite structure and hence the device becomes photodegradable.

In order to increase the stability of the perovskite device, the size of the A site cations must be bulky, i.e., longer chain A site cations. Due to the steric hindrance, the cations are not free to move. Longer chain A site cations were chosen within the specified tolerance range. In place of halide anions such as  $Cl^-$ , a mixture of two halide anions was utilized for analyzing the PCE of SCm known as mixed halide perovskites. Thus, by permutating organic and halide anionic sites without disturbing the tolerance factor, ionic migration was hindered leading to the enhancement of the intrinsic photo-stability. Increasing the photo-stability using different anionic and cationic sites with acceptable tolerance limits is

known as compositional mapping. However, opting for longer chain cationic sites might lead to distortion in the network with respect to various temperatures [124].

Bandgap tuning was performed to increase the light absorption without disturbing the absorption coefficient. Changing any of the A, B and X sites in ABX<sub>3</sub> will have a serious effect on the energy band gap. Altering any of the sites in the perovskite structure changes the tolerance factor, leading to a changed morphology of the crystal (Orthorhombic or Tetragonal or Cubic structure). This results in modification of the energy band gap of the perovskite PV cell [94]. Table 5 represents various perovskite materials with their energy band gaps. From the table, it is evident that changing any of the sites in perovskites alters the energy band gap from 2.3 eV to 1.3 eV. The performance of perovskite SC was improved by replacing the TiO<sub>2</sub> sheet with TiO<sub>2</sub> nanoparticles in a thin film as counter electrode. The stability of various compositions of perovskite SCs was evaluated through a humidity soaking test. Of various compositions, the humidity resistant composite perovskite based SC was considered for obtaining photocurrent generation at a higher rate [125].

**Table 5.** Energy gaps of various perovskite materials.

S.No	Material	HOMO Energy Level (eV)	LUMO Energy Level (eV)	Energy Bandgap (eV)
1	MAPbBr <sub>3</sub>	−5.68	−3.38	2.3
2	MAPbI <sub>3</sub>	−5.43	−3.88	1.55
3	FAPbI <sub>3</sub>	−5.42	−3.92	1.5
4	MAPb <sub>1-x</sub> Sn <sub>x</sub> I <sub>3</sub> (x = 0.25)	−5.48	−4.24	1.24
5	MAPb <sub>1-x</sub> Sn <sub>x</sub> I <sub>3</sub> (x = 0.5)	−5.61	−4.44	1.17
6	MAPb <sub>1-x</sub> Sn <sub>x</sub> I <sub>3</sub> (x = 0.75)	−5.77	−4.60	1.17
7	MASnI <sub>3</sub>	−5.47	−4.17	1.3

With the help of compositional mapping, there is a possibility of obtaining a 3D perovskite structure. As a result of band gap changes, there is a change in exciton generation leading to a more highly efficient perovskite device. The electronic properties of the perovskite material mainly depend on the heteropolar bond between the B and X sites. The size of the A site might show slight distortion in the heteropolar bonds, leading to change in the electronic properties of the perovskite device. The perovskite device structure can be fabricated as a mesoscopic nanostructure or a planar structure, stable only in the controlled environment. It starts degrading once exposed to the ambient conditions, due to thermal degradation, moisture sensitivity, intrinsic photo-instability, etc., [5]. For an ideal perovskite SC, thermal degradation and stability factors need to be more concentrated. Perovskite SC can be fabricated through solution-based and vapor-based approaches. The PV performance of perovskite SC was purely based on the concentration of A site cations. The simple perovskite SC is comprised of an electron transport layer, photoactive layer and hole transport layer [126].

The schematic diagram Figure 9 represents the simple architecture of the perovskite based SC. Table 6 collectively indicates the commonly used materials in perovskite SCs [127]. In general, the light becomes incident over the transparent conducting electrode. Initially, Indium Tin Oxide (ITO) was used as transparent electrode in perovskite technology. Due to their poor stability and higher cost of the indium element, there is a need to identify alternative materials as transparent electrode [126]. Fluorine Tin Oxide (FTO) was used as an alternative transparent conducting oxide for SCs. Then, the incoming light was transmitted into the hole transport layer. The electron and hole transport layer (copper thiocyanate) was selected based on its transparency, to allow incoming light and conduct the generated excitons to the external circuit. Here, sprinkled carbon enhances hole transportation, which is cheaper than using gold particles. Thereafter, the photons reach the absorber layer (perovskite layer), which is photoactive in nature. The photons with energy greater than the energy band gap of the absorber layer have the ability to generate electron-hole pairs.

Then, the electrons and holes are transferred to the external circuit through the electron transport layer ( $\text{TiO}_2$ ) and hole transport layer. The surface textures of electron transport materials (photoanodes), such as rods, cones, spheres or undefined micro-level shapes, also influence the PCE of SC [128]. Finally, excitons recombine at the photoactive layer.

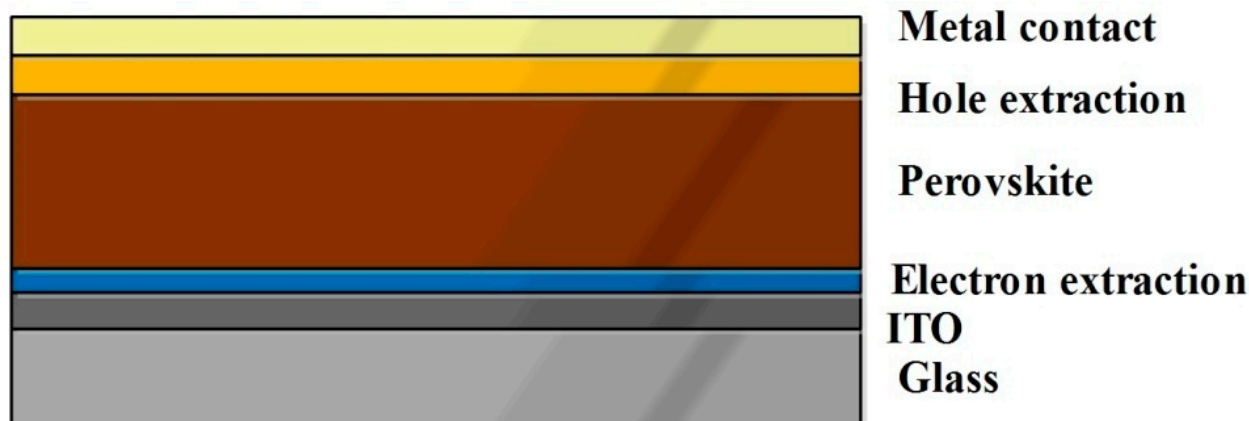


**Figure 9.** A schematic diagram represents the simple Perovskite Architecture.

**Table 6.** Most commonly used PSC part materials.

Various Interfacial Layers		Commonly Used Materials
Metal Contacts		Al, Au, Ag
Hole Transport Materials	Small molecules HTM	Spiro-OMeTAD, TPBC, OMe TPA-FA
	Polymer Based HTM	P3HT, PTAA, PEDOT:PSS
	Inorganic HTM	CuSCN, CuI, NiO, CuO
Perovskite materials		$\text{MAPb}(\text{I}_3, \text{Br}_3)$ , $\text{Cs}_2\text{AgBiBr}_6$ , $\text{FAPbI}_3$ , $\text{MASnI}_3$
Electron transport materials		ZnO, $\text{TiO}_2$ , PCBM, $\text{SnO}_2$
Conducting Oxide		ITO

Even though perovskite SCs have started to boom in the PV market, they also possess some disadvantages such as chemical instability, thermal instability, atmospheric moisture, excessive UV exposure, sealing issues and structural modifications [5]. Figure 10 represents the various stability issues occurring commonly in perovskite SCs. Distortion of crystals might influence the photoelectric parameters leading to degradation in crystallite perovskite structure. Temperature also influences the structural change in the crystal level. Table 7 represents the various structural modifications with respect to temperature change for various halogen ions.

**Table 7.** Structural changes of X site elements with respect to temperature change.

Element	Structural Change with Respect to the Temperature Variation ( $^{\circ}\text{C}$ )		
	Cubic	Tetragonal	Orthogonal
Iodine	>54.25	From 54.25 to $-110.95$	$<-110.95$
Bromine	> $-36.25$	From $-36.25$ to $-123.65$	$<-123.65$
Chlorine	> $-94.35$	From $-94.35$ to $-200.25$	$<-200.25$

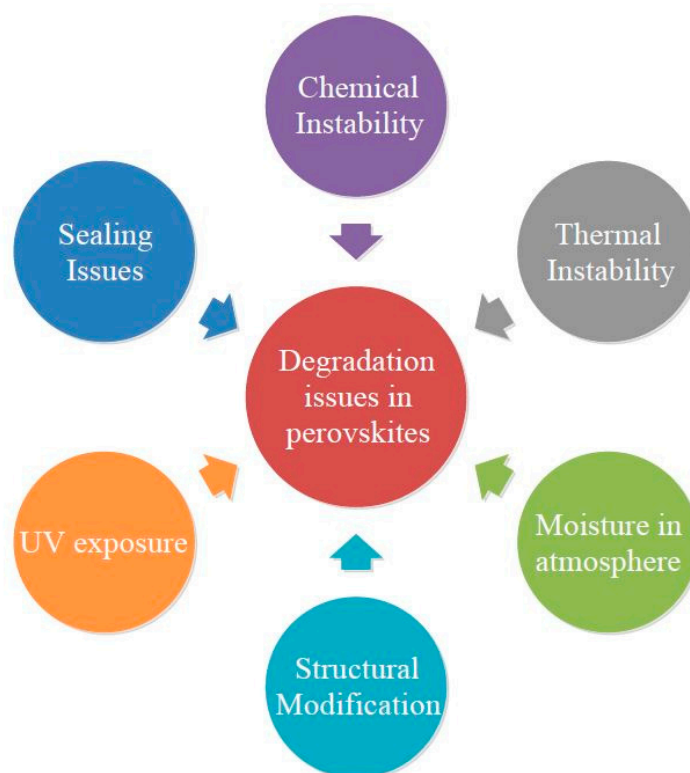


**Figure 10.** Various Stability Issues in Perovskite SCs.

Hole transport material is one of the predominant materials required for photocurrent generation. Changes in the chemical arrangement and structure of hole transport material leads to PSCs' instability [129]. Hence, PSCs without hole transport materials have the chance to avoid thermal instability. An appropriate percentage of atmospheric oxygen in contact with the perovskite structure leads to the oxidation of organic based components [130]. This further drives towards the degradation of elements from the cell architecture, lowering the cell's PCE. Improper sealing is prone to the inclusion of foreign materials with the elements of the various layers of the SC. This also decreases the performance of the PV cell. Suitable sealing materials such as UV curable resin and thin cavity glass material overcome foreign particle inclusion in the proposed device architecture [131]. Detailed comparison of various cell architectures of perovskite based SCs can be compared, along with their PV performance, in Table 8.

### 3.3. Organic Solar Cells

Only after the discovery of electrically conducting materials did organic SC enter the picture. In the case of organic SCs, the organic semiconducting polymers are crucial components because they lack prolonged chains. Smaller molecules have a lower molecular weight, whereas polymers have a much larger molecular weight [132]. These are semiconducting materials fabricated by a simple processing technique at lab scale, especially at lower temperatures. Between the organic molecules of conducting polymers along the carbon chain, there is a stronger bond, the  $\sigma$ -bond, while at the periphery the bonding is much weaker, referred to as  $\pi$ -bonds. There are two possible architectures which were noticed through various experimentation: normal and inverted architecture. In some circumstances, inverted architecture shows enhanced PCE compared to actual architecture [133]. The example of polymer-based cell architectures in normal and inverted structures are diagrammatically represented in Figures 11 and 12.

**Table 8.** Various perovskite based SCs with their PV parameters.

S.No	Photo-Absorber Material	Voc (mV)	Jsc (mA cm <sup>-2</sup> )	FF	PCE (%)	Ref.
1	(5-AVA) <sub>x</sub> (MA) <sub>1-x</sub> PbI <sub>3</sub> /ZrO <sub>2</sub> /TiO <sub>2</sub> & (5-AVA) <sub>x</sub> (MA) <sub>1-x</sub> PbI <sub>3</sub> /TiO <sub>2</sub>	740, 592	21.68, 12.51	0.64, 0.56	10.3, 4.18	[134]
2	CH <sub>3</sub> NH <sub>3</sub> PbI <sub>3</sub> /TiO <sub>2</sub> /Carbon	0.76, 0.89, 0.97 & 0.92	14.3, 15.1, 16.7 & 16.3	0.404, 0.415, 0.558 & 0.466	35, 51, 91 & 90	[135]
3	ITO/(PEDOT:PSS)/CH <sub>3</sub> NH <sub>3</sub> PbI <sub>3</sub> /PCBM/(0.5 nmLiF/Al)	0.846, 0.846	20.2, 19.2	0.767, 0.708	13.1, 11.5	[136]
4	ITO/PTAA/MA <sub>0.6</sub> FA <sub>0.38</sub> Cs <sub>0.02</sub> PbI <sub>2.975</sub> Br <sub>0.025</sub> :5 mol% MACl film/C60/BCP/Cu	1000	23.1	0.77	19.50	[137]
5	ITO/PEDOT:PSS/CH <sub>3</sub> NH <sub>3</sub> PbI <sub>3</sub> /C60/BCP/Al	780	19.7	0.736	11.30	[138]
6	FTO/TiO <sub>2</sub> /CH <sub>3</sub> NH <sub>3</sub> PbI <sub>3-x</sub> Cl <sub>x</sub> /spiro-MeOTAD/Ag	987, 946	18.72, 19.87	0.64, 0.6	12.14, 11.47	[139]
7	ITO/PEDOT:PSS/CH <sub>3</sub> NH <sub>3</sub> PbI <sub>3</sub> /PCBM/LiF-Ag	800, 950	15.89, 12.7	0.71, 0.64	9.05, 7.75	[140]
8	Glass/TCO/NiO/Perovskite/PCBM/PEI/Ag & Glass/TCO/NiO/Perovskite with 5% Cl/PCBM/PEI/Ag	1022, 1085	21.3, 21.2	0.71, 0.79	15.5, 18.2	[141]
9	FTO/TiO <sub>2</sub> Dense/TiO <sub>2</sub> /ZrO <sub>2</sub> /perovskite/Spheroidal graphite & FTO/TiO <sub>2</sub> Dense/TiO <sub>2</sub> /ZrO <sub>2</sub> /perovskite/Flaky graphite	878, 825	12.4, 10.6	0.61, 0.46	6.64, 4.08	[142]
10	FTO/FAPbI <sub>3</sub> /Spiro-OMeTAD/Au	970	21.6	0.62	13	[143]
11	FTO/TiO <sub>2</sub> /CH <sub>3</sub> NH <sub>3</sub> PbI <sub>3</sub> /spiro-oMeTAD/Au	1090 & 1090	23.50 & 17.62	0.61 & 0.69	11.70 & 17.71	[144]
12	FTO/TiO <sub>2</sub> /(FAPbI <sub>3</sub> ) <sub>0.85</sub> (MAPbBr <sub>3</sub> ) <sub>0.15</sub> /PTAA/Ag & FTO/TiO <sub>2</sub> /(FAPbI <sub>3</sub> ) <sub>0.85</sub> (MAPbBr <sub>3</sub> ) <sub>0.15</sub> /PCBM/BCP/In	1010, 1010	23.20, 22.34	0.7858 & 0.7826	20.05 & 19.23	[145]



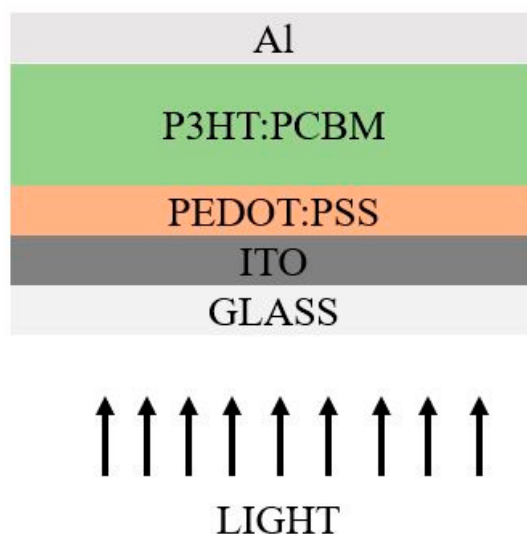


**Figure 11.** Actual Architecture.

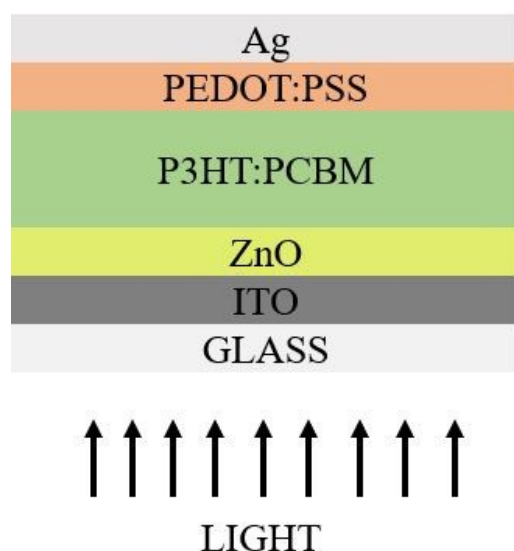


**Figure 12.** Inverted Architecture.

The electrical conductivity in polymers mainly occurs through  $\pi$ -bonds. This is possible through appropriate doping of material with organic compounds. Doping of external elements easily delocalizes the  $\pi$ -electrons regarding their mobility. For instance, Sulphur doping in polymers easily delocalizes the  $\pi$ -electrons regarding their mobility. For instance, Sulphur doping in polymers transforms the benzene into thiophene which facilitates electrical conductivity in polymers along the  $\pi$  channel. Due to the doping of external elements with polythiophene, pentacene, etc., maintaining an extended  $sp_2$  hybridization state facilitates electron transfer [146]. Hence, they are called  $\pi$ -conjugated materials. The dopants were responsible for improved electrical conductivity.  $SO_3CF_3^-$  dopant in polythiophene and  $FeCl_3$  dopant in poly-pyrrole lead to increased electrical conductivities of 10–20 S/cm and 3–200 S/cm. Such materials are employed as basic elements of organic electronic devices [147].

Among them, organic SCs are one of the most promising. In general, the polymeric SCs were mostly preferred, because synthesis of small molecules is a tedious process via the solution processing technique [148]. Smaller molecules such as pentacene can also be easily evaporated, but polymers such as Poly3-hexyl Thiophene ( $P_3HT$ ) cannot be. Polymer based SCs are easily fabricated. Compared to the workflow of the normal p-n junction SC, the major drawbacks of polymer SCs are complex exciton dissociation due to higher binding energy

and transport, diffusion, and dissociation of the exciton. The exciton possess and shorter diffusion length, and they should dissociate before recombination [149]. For inorganic SCs, binding energy of the exciton will be approximately equal to thermal energy, while the exciton binding energy of organic SCs might be 0.2 to 0.3 e V. Thus, the junction materials were chosen based on an adequate electric field to overcome the binding energy. Organic SCs are mostly synthesized at the lab scale, hence their properties can be tuned easily.

Some of the advantages are [150]:

- easy to synthesize
- available at low cost
- high degree of tunability
- high absorption coefficient
- flexible in nature.

Major disadvantages of the Organic SCs are:

- high exciton binding energy
- low carrier diffusion lengths
- low strength and stability.

Due to their higher absorption coefficient property, the thickness must be increased for obtaining the intensified light traction. Due to the lower carrier diffusion length, there is a very low possibility of increasing the thickness of the SC. These properties are contradictory with each other and hence optimal thickness must be predicted without disturbing the absorption coefficient and carrier diffusion length for better performance of the SC [151]. There are three possible cell architectures for organic SC.

### 3.3.1. Single Layer Device

The polymer SC material is a-periodic in nature. Hence, its energy bands are referred to as Lowest Unoccupied Molecular Orbital (LUMO) and Highest Occupied Molecular Orbital (HOMO). LUMO and HOMO might be equivalent to the conduction band edge and valence band edge. Here, the electrons were excited from HOMO to LUMO. A working strategy for a single layer device includes: formation of exciton, diffusion of exciton towards the nearer electrode and dissociation of exciton at the interface, holding adequate energy for dissociation [152]. They are very thin in nature and possess a shorter diffusion length, making it difficult to absorb much more sunlight. As a result, quantum efficiency of the device is lower and there is a risk of optimizing the thickness of the organic semiconductor. The drawbacks of the single layer devices are overcome through bilayer devices [153].

### 3.3.2. Bilayer Devices

Bilayer SCs possess a donor (photoactive layer), an acceptor, two electrodes and carrier selective layers. Bilayer devices generally have carrier selective layers for ensuring that the specific carrier reaches the electrode. When light is incident over the donor material, the excitons generated move towards the interfacial region of donor and acceptor [154]. Donors can absorb light more effectively than acceptors. Due to the difference in the energy levels of HOMO and LUMO of donor and acceptor, there will be an internal electric field which releases excitons into the free charge carriers. The PCE of the bilayer device is higher than that of single layered devices (4–5%) because of its hetero-junctive nature. Due to the lower device thickness, light absorption is limited to a certain extent, which is rectified through bulk heterojunction SCs [155].

### 3.3.3. Bulk Heterojunction Device

A bulk heterojunction device is a mixture of p- and n- type materials in nanoscale. Hence, the exciton readily finds the interface capable of providing an adequate electric field to break up the exciton into charge carriers. The network of two phases (p & n type) is continuous, thus there is a continuous flow of charge carriers through the external circuit. A built-in electric field is developed at the interfacial area for effective breaking

of the excitons [156]. By increasing the interfacial area, the exciton finds an interface before recombination. With the intermixing of p & n types, the probability of finding the interface within the diffusion length is higher. There are two possible cell architectures: actual and inverted architecture. Inverted architecture can sometimes show enhanced cell performance [157]. The comparison of various polymeric materials used as a photo absorber layer, along with cell performance, is tabulated in Table 9.

In general, inorganic polymer SCs possess enhanced stability, but bulk heterojunction structured polymer SCs have certain difficulties in controlling side chain orientation and entanglement [158]. A p-i-n structure might enhance the performance of the bulk heterojunction, as it shows an increased internal magnetic field and mechanical stability when subjected to thermal stresses. p-i-n structures also hold better strength and hence are generally preferred [159]. Polymer acceptors play a vital role in photo electric generation. If they possess larger crystals, this might lead to phase separation at a larger scale. This in turn is reduced by the introduction of the fluorinated copolymer. This results in fewer crystal boundaries and increased exciton mobility. The addition of copolymers in a calculated quantity enhances the flexibility of polymer based SCs [160].

**Table 9.** Representation of various polymer based SCs with their cell performances.

S.No	Cell Architecture	Voc	Jsc	FF	Eff	Ref.
1	Glass/ITO/PEDOT:PSS/(CD1:PBN-12)/LiF/Al	1017	13.39	0.64	10.1	[161]
2	ITO/ZnO/PTQ11–TPT10/MoO <sub>3</sub> /Ag	880	24.79	0.74	16.32	[162]
3	glass/ITO/PEDOT:PSS/active layers/PDIN	854	23.01	72.27	14.2	[163]
4	ITO/PEDOT:PSS/active layer/PDIN/Al	0.853	25.68	78.61	17.22	[164]
5	glass/ITO/PEDOT:PSS/active layer/PDINO/Al	826	26.65	75.1	16.53	[165]
6	(ITO)/ZnO/J71:ITIC:BTF/MoO <sub>3</sub> /Ag.	952	18.48	70.03	12.35	[166]
7	glass/ITO/PEDOT: PSS/PM6: PT-IDTTICr (8: 5.3 mg mL <sup>-1</sup> in CHCl <sub>3</sub> )/PFN/Al	970	18.19	68	12.06	[167]
8	Active layer-ITCF3/PM6	840	20.9	76	13.3	[168]
9	20% wt of IT-4F acceptor	844	25.4	75.9	16.27	[169]
10	ITO/PEDOT:PSS/Pt10:Y6/OTF/Al	810	26.45	76.3	16.35	[153]
11	ITO/PEDOT:PSS/PM6:PFBDT-IDTIC/PNDITF3N-Br/Al	960	15.38	69	10.3	[170]
12	ITO/PEDOT:PSS/PM6:PZ1/ZnO/Al	960	17.1	68.2	11.2	[171]

### 3.4. Quantum Dots Solar Cells

QD SCs have a tendency to improve the photogeneration process through pre-designed QD arrays. CdX was extensively involved in the research of QDs because of its enhanced electrochemical and optical properties. X site elements may be S, Se, Te, etc. Density of state is defined as the number of available energy states per unit energy per unit volume. The total integral of the Fermi distribution function with maximum and minimum energy intervals results in the total number of electrons or holes present in the corresponding energy band. Whenever the dimension of the material changes, there is a significant change in the corresponding density of states [172]. This indicates the number of available charge carriers for occupancy. At particular energy state E, the probability of electron states' occupancy by an electron is determined through the probability distribution function [173].

Semiconducting materials which provide response to incident light were fabricated as QDs for achieving higher output performance through an easily tunable energy band gap [174]. The minimal optical density of thin film QDs was improved by the quantity of light passed through it. Some of the nanostructures developed to transform the semiconducting materials were nanosheets, nanorods, nanowires, etc. The QDs were sensitized due

to light incidence and the redox electrolyte adheres over the surface of the QDs, facilitating the electron and ion movement [175]. The stability of QDSCs depends on the type of electrolytes used and the method of recombination and extraction of holes from QDs. In the case of DSSCs, inorganic as well as amorphous coatings, made to adhere over the counter electrode TiO<sub>2</sub>, deliver a consistent current output irrespective of the corrosive electrolyte (I<sup>-</sup>/I<sub>3</sub><sup>-</sup> redox couple) utilized for charge carrier transfer [176].

The generated electrons will be transferred to the conduction band of the semiconductor through the TCO electrode to reach the external circuit. The holes generated in the conduction band of QDs were regenerated with the help of I<sup>-</sup>/I<sub>3</sub><sup>-</sup> redox couple. Because of the quantum confinement effect, discrete energy band gaps were found to be easily tunable in nature, especially in excited states [177]. The generated electrons might access any of the energy levels, hence electron excitation from the ground state is multi-poled. Table 10 represents the various density of states and the motion of electrons for differently dimensioned materials. The device architecture represented in Figure 13 shows the simple QD based SC structure. Here, the light entering through the counter electrode mainly assists the hole transportation [178]. Then HTM adheres to the redox couple (I<sup>-</sup>/I<sub>3</sub><sup>-</sup> couple) which is responsible for transfer of the generated holes. Following this phenomenon, QDs adsorbed with the TiO<sub>2</sub> film (photo absorber material) are chosen for exciton generation. The conductive glass substrate, such as FTO glass, is placed next to the photo active material responsible for transfer of generated electrons through the external circuit [179].

**Table 10.** Comparison of density of states and motion of electrons for various dimensioned materials.

S.No	Type of Material	Density of States	Motion of Electron
1	3D (Bulk material)	$\sqrt{E}$	Free to move in all directions
2	2D (Quantum Well)	$E^0$	Restricted to two directions
3	1D (Quantum Wire)	$\frac{1}{\sqrt{E}}$	Restricted to one direction
4	0D (QD)		Restricted in all directions

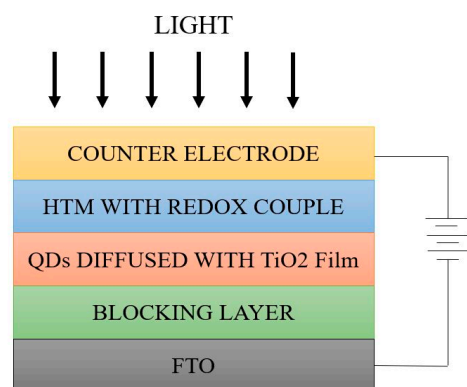


**Figure 13.** Device architecture of QD SC.

Dimensionality of a material defines the motion of generated electrons in various directions. Density of states helps to determine carrier energy distribution and concentration of carriers. QDs are tiny-sized semiconductor particles with electronic and optical properties which are entirely different from larger-sized LED particles. Energy band gaps of QDs can be tuned easily by changing their shape, size and material. With the change of material and size, the photoemission property also changes. They are also referred to as artificial atoms because they hold discrete electronic states similar to naturally occurring atoms. QDs are generally intermediate between the discrete atoms and bulk semiconductors [180]. Their optoelectronic property changes in accordance with the size and shape of QDs. Large sized QDs emit lights of longer wavelength, while smaller sized QDs emit lights of shorter wavelength. However, the color of light emitted is purely based on the composition of

the QDs. Due to their enhanced tunable property, QDs find application in the field of SCs, LEDs, transistors, diode-based lasers, medical imaging, etc. QDs are fabricated through the following techniques: lithography, colloidal synthesis and epitaxy. QD synthesis requires a longer time period, ranging from liquid phase methods to vapor phase epitaxial growth techniques [181]. The QDs are deposited on the electrode surface through electrophoretic deposition, spin coating, drop casting, chemical bath deposition, bifunctional linker approach, etc., Among these, spin coating and the drop casting deposition technique are simple coating and drying methods for synthesized colloidal QDs. The chemical bath deposition technique requires precursors involving chemical reaction with the colloidal solution, while electrophoretic deposition requires a DC electric field applied between the electrodes dipped into the QD solution. Non-polar and polar solvent drives the negatively charged QD particles towards the electrode surface [182].

In the lithography technique, a carbon copy (pattern) of the shape to be obtained is initially generated [183]. Some of the types of lithography are electron beam lithography, photolithography, ion beam lithography and X-ray lithography. In order to create a pattern, an electron beam and light are used in electron beam and photo lithography [184]. For the fabrication of QDs, the electron beam or ion beam lithography technique is usually preferred, which is similar to quantum well fabrication. In quantum well fabrication, a polymer mask is covered in accordance with the required pattern [185]. The electron or ion beam is exposed gradually for etching of the unwanted surfaces. The main disadvantages of this method are easy formation of defect or trap states, much lower density, proneness to easier contamination and longer operating time [186].

The epitaxy-pattern growth technique is used to grow the lower bandgap material over the surface of the larger bandgap material. For example, GaAs were grown over the surface of AlGaAs material. Here, the growth of substrate was hindered by masking compound coating [187]. The main disadvantage of this method is the density and number of QDs influenced by the mask pattern used. In epitaxy-self organized growth technique, epitaxy was grown based on the lattice constant of the substrate and the type of crystallizing material [188]. Whenever the thickness of the crystallized layer is higher than the critical thickness, then there is an occurrence of stronger strain over the layers. As a result, breakdown occurs leading to the formation of randomly distributed islets of predefined size and shape. The main disadvantages of this method are more fluctuations in the size, shape and arrangement of layers [189].

Colloidal synthesis of QDs is a technique resulting in bulk material formation. There is also a possibility of printing over flexible substrates through a roll-to-roll technique. During the liquid and vapor phase synthesis, the liquid phase technique has the capability of producing highly dispersed QDs in various solutions [190]. For instance, heating of specific organic solvents followed by forced injection of semiconductor precursors results in the synthesis of QDs. Depending upon the time interval for the heating process and the required quantity of precursors, the distribution of various sizes and shapes of QDs is achieved [191]. In the case of CdSeQDs synthesis, the Cd and Se precursors such as  $\text{Cd}(\text{CH}_3)_2$  and elemental Se are taken in the presence of surfactant or stabilizing agent (tri-n-octyl-phosphine) solutions mixed together and then injected into heated tri-octyl-phosphine oxide solution under an inert atmosphere in a three necked conical flask [192]. A series of QDs was obtained at a temperature of 320 °C for a few hours. Compared to the bulk material, the QDs were capable of generating more excitons, resulting in enhanced PCE and PV performance [193]. The PCE can be enhanced by decreasing the possibility of exciton recombination through surface passivation of the photo electrodes to which the QDs were adhered through wider band gap semiconducting materials [194]. The coating thickness of the passivating layer controls the hole transfer. If thickness of coating is higher than the passivating layer, hole transfer is hindered. Thus, the optimal passivating layer thickness should be decided initially [195]. Table 11 represents various QDs in QDSCs with their corresponding output cell efficiency.

**Table 11.** Comparing the various QDs in QDSCs with respect to surface passivation and obtained cell efficiency.

S.No	QD Material	Voc	Jsc	FF	Eff (%)	Ref.
1	CdSe	710	7.51	0.5	2.7	[194]
2	CuInS <sub>2</sub> -Mn doped CdS	581	19.29	0.48	5.38	[195]
3	CdSeTe	653	20.78	0.605	8.21	[196]
4	CdSeTe with ZrOCl <sub>2</sub> treatment	21.04	72	0.642	9.73	[197]
5	PbS/CdS	416	22	0.453	4.2	[198]
6	CIS	586	20.65	0.581	7.04	[199]
7	ZnTe/CdSe	642	19.65	0.57	7.17	[200]
8	Cu <sub>0.23</sub> In <sub>0.36</sub> Te <sub>0.19</sub> Se <sub>0.22</sub>	400	17.4	0.44	3.1	[201]
9	CdS/CdSe	575	13.68	0.63	4.92	[202]
10	InAs/GaAs with Si doping	840	27.6	0.734	17	[203]

Some of the advantages of QDSCs are:

- Higher output performance with minimal fabrication cost.
- Minimal area required for more power output.
- Flexible nature leading to easier incorporation in any curvatures.
- Lesser weight.

Some of the disadvantages noticed in QDSCs are:

- Under the inclusion of moisture and UV radiation, degradation of QDs was found to be higher.
- Shells in atomic configuration may modify the optical properties, and hence the size of particles is harder to control
- CdSe QDs are more toxic in nature.

#### 4. Conclusions

Thin-film SC modules are rapidly entering the market, providing a chance for these potentially lower-cost techniques to prove their credentials. Several unique thin-film technologies, based on silicon in amorphous, polycrystalline, or mixed phases, or on chalcogenides, are presently available or nearing completion. More research has been conducted on first-generation SCs. As a result, the second and third generation SCs were evaluated based on their operating mechanism, various materials utilized in the cell, fundamental properties, and so on. This review paper will help scholars and industrialists to understand the current challenges and progress in thin-film SCs. This also allows researchers to experiment with hybrid heterojunction SCs and tandem SCs. In addition, possible manufacturing procedures have been considered. Each SC has distinct characteristics and has been used in a variety of situations. However, high efficiency SCs are most likely discovered to be multi junction SCs in the future because they can convert a larger spectrum of incoming light to solar energy than any other solar design. The majority of the PCE indicated for various solar materials were acquired exclusively at the lab scale. The major problem in solar PV technology is successfully transitioning from laboratory to large-scale manufacture. This is a time-consuming process that needs significantly more extra funding.

**Author Contributions:** Conceptualization, S.S., R.R. and G.V.K.; methodology, R.R., G.V.K. and H.P.; software, S.S. and R.R.; validation, H.P., Z.S., A.J.A. and M.M.J.; formal analysis, S.S., A.J.A., M.M.J., G.V.K., S.M. and Z.S.; investigation, S.S., R.R., H.P. and A.J.A.; resources, S.S., R.R., G.V.K., H.P., Z.S. and S.M.; data curation, S.S., R.R., M.M.J. and Z.S.; writing—original draft preparation, S.S., R.R., G.V.K., H.P., A.J.A. and M.M.J.; writing—review and editing, S.M., Z.S. and H.P.; visualization, S.S., R.R., M.M.J., A.J.A. and Z.S.; supervision, H.P. and G.V.K.; project administration, H.P., Z.S. and S.M.;



funding acquisition, Z.S. and S.M. All authors have read and agreed to the published version of the manuscript.

**Funding:** This research received no external funding.

**Data Availability Statement:** Not applicable.

**Acknowledgments:** The author V. K. Gobinath thanks the Science and Engineering Research Board (SERB), Government of India, for the final completion of this research work through the Teachers Associateship for Research Excellence (Ref No. TAR/2021/000173).

**Conflicts of Interest:** Authors declare that there is no conflict of interest.

## References

1. Pansal, K.; Ramani, B.; kumar Sadasivuni, K.; Panchal, H.; Manokar, M.; Sathyamurthy, R.; Israr, M. Use of solar photovoltaic with active solar still to improve distillate output: A review Groundwater sustain. *Develop* **2020**, *10*, 100341.
2. Anand, A.; Shukla, A.; Panchal, H.; Sharma, A. Thermal regulation of photovoltaic system for enhanced power production: A review. *J. Energy Storage* **2021**, *35*, 102236. [[CrossRef](#)]
3. Pandiaraj, S.; Jaffar, A.A.; Muthusamy, S.; Panchal, H.; Pandiyan, S. A study of solar heat gain variation in building applied photovoltaic buildings and its impact on environment and indoor air quality. *Energy Sources Part A Recovery Util. Environ. Eff.* **2022**, *44*, 6192–6212. [[CrossRef](#)]
4. Shah, A.; Platz, R.; Keppner, H. Thin-film silicon solar cells: A review and selected trends. *Sol. Energy Mater. Sol. Cells* **1995**, *38*, 501–520. [[CrossRef](#)]
5. Asghar, M.; Zhang, J.; Wang, H.; Lund, P. Device stability of perovskite solar cells—A review. *Renew. Sustain. Energy Rev.* **2017**, *77*, 131–146. [[CrossRef](#)]
6. Santhosh, S.; Rajasekar, R.; Gobinath, V.; Moganapriya, C.; Arun Kumar, S.; Manju Sri, A. Influence of Electrospayed MoSe2 Antireflective Surface Coatings on Performance of Multicrystalline Silicon Solar Cell. *Silicon* **2022**, *14*, 6039–6051. [[CrossRef](#)]
7. Chinnasamy, M.; Rathanasamy, R.; Sivaraj, S.; Velu Kaliyannan, G.; Palanisamy, M.; Pal, S.K.; Uddin, M. Effective Utilization of Synthesized FeS<sub>2</sub> for Improving Output Performance of Polycrystalline Silicon Solar Cell. *Adv. Mater. Sci. Eng.* **2022**, *2022*, 1252105. [[CrossRef](#)]
8. Rathanasamy, R.; Velu Kaliyannan, G.; Sivaraj, S.; Saminathan, A.; Krishnan, B.; Palanichamy, D.; Uddin, M. Influence of Silicon Dioxide-Titanium Dioxide Antireflective Electrospayed Coatings on Multicrystalline Silicon Cells. *Adv. Mater. Sci. Eng.* **2022**. [[CrossRef](#)]
9. Lee, Y.; Park, C.; Balaji, N.; Lee, Y.J.; Dao, V.A. High-efficiency silicon solar cells: A review. *Isr. J. Chem.* **2015**, *55*, 1050–1063. [[CrossRef](#)]
10. Menna, P.; Di Francia, G.; La Ferrara, V. Porous silicon in solar cells: A review and a description of its application as an AR coating. *Sol. Energy Mater. Sol. Cells* **1995**, *37*, 13–24. [[CrossRef](#)]
11. Lal, N.N.; Dkhisssi, Y.; Li, W.; Hou, Q.; Cheng, Y.B.; Bach, U. Perovskite tandem solar cells. *Adv. Energy Mater.* **2017**, *7*, 1602761. [[CrossRef](#)]
12. Bouich, A. *Study and Characterization of Hybrid Perovskites and Copper-Indium-Gallium Selenide Thin Films for Tandem Solar Cells*; Universitat Politècnica de València: Valencia, Spain, 2021.
13. Mahmood, A. Triphenylamine based dyes for dye sensitized solar cells: A review. *Sol. Energy* **2016**, *123*, 127–144. [[CrossRef](#)]
14. De Wolf, S.; Descoeurdes, A.; Holman, Z.C.; Ballif, C. High-efficiency silicon heterojunction solar cells: A review. *Green* **2012**, *2*, 7–24. [[CrossRef](#)]
15. Chopra, K.; Paulson, P.; Dutta, V. Thin-film solar cells: An overview. *Prog. Photovolt. Res. Appl.* **2004**, *12*, 69–92. [[CrossRef](#)]
16. Shah, A.; Torres, P.; Tscharnner, R.; Wyrsh, N.; Keppner, H. Photovoltaic technology: The case for thin-film solar cells. *Science* **1999**, *285*, 692–698. [[CrossRef](#)]
17. Carlson, D.E.; Wronski, C.R. Amorphous silicon solar cell. *Appl. Phys. Lett.* **1976**, *28*, 671–673. [[CrossRef](#)]
18. Elsayed, H.A.; Sayed, H.; Taha, T.; Alharbi, A.G.; Alenad, A.M.; Alshammari, B.A.; Ahmed, A.M.; Mehaney, A.; Aly, A.H. Simple and efficient design towards a significant improvement of the optical absorption of amorphous silicon solar cell. *J. Quant. Spectrosc. Radiat. Transf.* **2021**, *275*, 107890. [[CrossRef](#)]
19. Eminian, C.; Haug, F.J.; Cubero, O.; Niquille, X.; Ballif, C. Photocurrent enhancement in thin film amorphous silicon solar cells with silver nanoparticles. *Prog. Photovolt. Res. Appl.* **2011**, *19*, 260–265. [[CrossRef](#)]
20. Liu, W.; Shi, J.; Zhang, L.; Han, A.; Huang, S.; Li, X.; Peng, J.; Yang, Y.; Gao, Y.; Yu, J. Light-induced activation of boron doping in hydrogenated amorphous silicon for over 25% efficiency silicon solar cells. *Nat. Energy* **2022**, *7*, 427–437. [[CrossRef](#)]
21. Krč, J.; Zeman, M.; Kluth, O.; Smole, F.; Topič, M. Effect of surface roughness of ZnO: Al films on light scattering in hydrogenated amorphous silicon solar cells. *Thin Solid Film.* **2003**, *426*, 296–304. [[CrossRef](#)]
22. Baek, S.; Lee, J.C.; Lee, Y.-J.; Iftiqar, S.S.; Kim, Y.; Park, J.; Yi, J. Interface modification effect between p-type a-SiC: H and ZnO: Al in pin amorphous silicon solar cells. *Nanoscale Res. Lett.* **2012**, *7*, 1–5. [[CrossRef](#)] [[PubMed](#)]
23. Sihanugrist, P.; Sasaki, T.; Asano, A.; Ichikawa, Y.; Sakai, H. Amorphous silicon oxide and its application to metal/nip/ITO type a-Si solar cells. *Sol. Energy Mater. Sol. Cells* **1994**, *34*, 415–422. [[CrossRef](#)]

24. Theuring, M.; Geissendörfer, S.; Vehse, M.; von Maydell, K.; Agert, C. Thin metal layer as transparent electrode in nip amorphous silicon solar cells. *EPJ Photovolt.* **2014**, *5*, 55205. [[CrossRef](#)]
25. Yue, G.; Han, D.; Williamson, D.; Yang, J.; Lord, K.; Guha, S. Electronic states of intrinsic layers in nip solar cells near amorphous to microcrystalline silicon transition studied by photoluminescence spectroscopy. *Appl. Phys. Lett.* **2000**, *77*, 3185–3187. [[CrossRef](#)]
26. Kwak, J.; Kwon, S.W.; Lim, K.S. Fabrication of an-p-p tunnel junction for a protocrystalline silicon multilayer/amorphous silicon tandem solar cell. *J. Non-Cryst. Solids* **2006**, *352*, 1847–1850. [[CrossRef](#)]
27. Myong, S.Y.; Kwon, S.W.; Lim, K.S.; Konagai, M. Highly stabilized protocrystalline silicon multilayer solar cell using a silicon-carbide double p-layer structure. *Sol. Energy Mater. Sol. Cells* **2005**, *85*, 133–140. [[CrossRef](#)]
28. Kim, K.-H.; Johnson, E.V.; Cabarrocas, P.R. Irreversible light-induced degradation and stabilization of hydrogenated polymorphous silicon solar cells. *Sol. Energy Mater. Sol. Cells* **2012**, *105*, 208–212. [[CrossRef](#)]
29. Street, R.A. *Hydrogenated Amorphous Silicon*; Cambridge University Press: Cambridge, UK, 2005.
30. Lee, T.D.; Ebong, A.U. A review of thin film solar cell technologies and challenges. *Renew. Sustain. Energy Rev.* **2017**, *70*, 1286–1297. [[CrossRef](#)]
31. Sai, H.; Matsui, T.; Matsubara, K.; Kondo, M.; Yoshida, I. 11.0%-efficient thin-film microcrystalline silicon solar cells with honeycomb textured substrates. *IEEE J. Photovolt.* **2014**, *4*, 1349–1353. [[CrossRef](#)]
32. Pakala, P.S.A.; Pattnaik, A.; Tomar, A. Comprehensive Study on Heterojunction Solar Cell. In *Machine Learning, Advances in Computing, Renewable Energy and Communication*; Springer: Berlin, Germany, 2022; pp. 543–552.
33. Liu, H.; Du, Y.; Yin, X.; Bai, M.; Liu, W. Micro/Nanostructures for Light Trapping in Monocrystalline Silicon Solar Cells. *J. Nanomater.* **2022**, *2022*, 8139174. [[CrossRef](#)]
34. Stannowski, B.; Gabriel, O.; Calnan, S.; Frijnts, T.; Heidelberg, A.; Neubert, S.; Kirner, S.; Ring, S.; Zelt, M.; Rau, B. Achievements and challenges in thin film silicon module production. *Sol. Energy Mater. Sol. Cells* **2013**, *119*, 196–203. [[CrossRef](#)]
35. Yan, D.; Phang, S.P.; Wan, Y.; Samundsett, C.; Macdonald, D.; Cuevas, A. High efficiency n-type silicon solar cells with passivating contacts based on PECVD silicon films doped by phosphorus diffusion. *Sol. Energy Mater. Sol. Cells* **2019**, *193*, 80–84. [[CrossRef](#)]
36. Benagli, S.; Borrello, D.; Vallat-Sauvain, E.; Meier, J.; Kroll, U.; Hötzel, J.; Bailat, J.; Steinhauser, J.; Marmelo, M.; Monteduro, G. High-efficiency amorphous silicon devices on LPCVD-ZnO TCO prepared in industrial KAI-M R&D reactor. In Proceedings of the 24th European Photovoltaic Solar Energy Conference, Hamburg, Germany, 21–25 September 2009; pp. 21–25.
37. Matsui, T.; Maejima, K.; Bidiville, A.; Sai, H.; Koida, T.; Suezaki, T.; Matsumoto, M.; Saito, K.; Yoshida, I.; Kondo, M. High-efficiency thin-film silicon solar cells realized by integrating stable a-Si: H absorbers into improved device design. *Jpn. J. Appl. Phys.* **2015**, *54*, 08KB10. [[CrossRef](#)]
38. Matsui, T.; Sai, H.; Saito, K.; Kondo, M. High-efficiency thin-film silicon solar cells with improved light-soaking stability. *Prog. Photovolt. Res. Appl.* **2013**, *21*, 1363–1369. [[CrossRef](#)]
39. Banerjee, A.; Su, T.; Beglau, D.; Pietka, G.; Liu, F.S.; Almutawalli, S.; Yang, J.; Guha, S. High-efficiency, multijunction nc-Si: H-based solar cells at high deposition rate. *IEEE J. Photovolt.* **2012**, *2*, 99–103. [[CrossRef](#)]
40. Sai, H.; Koida, T.; Matsui, T.; Yoshida, I.; Saito, K.; Kondo, M. Microcrystalline silicon solar cells with 10.5% efficiency realized by improved photon absorption via periodic textures and highly transparent conductive oxide. *Appl. Phys. Express* **2013**, *6*, 104101. [[CrossRef](#)]
41. Sai, H.; Matsui, T.; Koida, T.; Matsubara, K.; Kondo, M.; Sugiyama, S.; Katayama, H.; Takeuchi, Y.; Yoshida, I. Triple-junction thin-film silicon solar cell fabricated on periodically textured substrate with a stabilized efficiency of 13.6%. *Appl. Phys. Lett.* **2015**, *106*, 213902.
42. Ramanujam, J.; Bishop, D.M.; Todorov, T.K.; Gunawan, O.; Rath, J.; Nekovei, R.; Artegiani, E.; Romeo, A. Flexible CIGS, CdTe and a-Si: H based thin film solar cells: A review. *Prog. Mater. Sci.* **2020**, *110*, 100619. [[CrossRef](#)]
43. Ramanujam, J.; Singh, U.P. Copper indium gallium selenide based solar cells—a review. *Energy Environ. Sci.* **2017**, *10*, 1306–1319. [[CrossRef](#)]
44. Nicolaou, C.; Zacharia, A.; Delimitis, A.; Itskos, G.; Giapintzakis, J. Single-step growth of high quality CIGS/CdS heterojunctions using Pulsed Laser Deposition. *Appl. Surf. Sci.* **2020**, *511*, 145547. [[CrossRef](#)]
45. Yamaguchi, T.; Ogawa, H.; Nakashima, M.; Naoi, H.; Araki, H.; Jimbo, K.; Katagiri, H.; Sasano, J.; Izaki, M. Fabrication of Cu<sub>2</sub>ZnSn (S, Se) 4 thin-film solar cells by sulfurization using Cu<sub>2</sub>ZnSnSe<sub>4</sub>, NaF and KF compounds. *Jpn. J. Appl. Phys.* **2020**, *59*, SGGF11. [[CrossRef](#)]
46. Kaliyannan, G.V.; Rathanasamy, R.; Sivaraj, S.; Chinnasamy, M.; Kandasamy, S. An Extensive Review Owing to the Influence of Surface Coating on the Technical Performance of Solar Cells. *Adv. Funct. Smart Mater.* **2022**, 13–23. [[CrossRef](#)]
47. Mufti, N.; Amrillah, T.; Taufiq, A.; Diantoro, M.; Nur, H. Review of CIGS-based solar cells manufacturing by structural engineering. *Sol. Energy* **2020**, *207*, 1146–1157. [[CrossRef](#)]
48. Bensaad, A.; Garadi, A.; Beloufa, A.; Bensaad, Z. Efficiency enhancement of Cd-free buffer layers on CIGS solar cell performance using WxAMPS. *Optik* **2022**, *267*, 169736. [[CrossRef](#)]
49. Zouache, R.; Bouchama, I.; Saidani, O.; Djedoui, L.; Zaidi, E. Numerical study of high-efficiency CIGS solar cells by inserting a BSF  $\mu\text{c-Si: H}$  layer. *J. Comput. Electron.* **2022**, *21*, 1386–1395. [[CrossRef](#)]
50. Kamada, R.; Yagioka, T.; Adachi, S.; Handa, A.; Tai, K.F.; Kato, T.; Sugimoto, H. New world record Cu (In, Ga)(Se, S)<sub>2</sub> thin film solar cell efficiency beyond 22%. In Proceedings of the 2016 IEEE 43rd Photovoltaic Specialists Conference (PVSC), Portland, OR, USA, 5–10 June 2016; pp. 1287–1291.

51. Powalla, M.; Paetel, S.; Ahlswede, E.; Wuerz, R.; Wessendorf, C.D.; Magorian Friedlmeier, T. Thin-film solar cells exceeding 22% solar cell efficiency: An overview on CdTe-, Cu (In, Ga) Se<sub>2</sub>-, and perovskite-based materials. *Appl. Phys. Rev.* **2018**, *5*, 041602. [[CrossRef](#)]
52. Youn, S.-M.; Park, M.-J.; Kim, J.H.; Jeong, C. Performance enhancement of CIGS thin-film solar cells with a functional-window NiO thin layer. *J. Alloy. Compd.* **2020**, *836*, 154803. [[CrossRef](#)]
53. Zhao, Y.; Yuan, S.; Kou, D.; Zhou, Z.; Wang, X.; Xiao, H.; Deng, Y.; Cui, C.; Chang, Q.; Wu, S. High Efficiency CIGS Solar Cells by Bulk Defect Passivation through Ag Substituting Strategy. *ACS Appl. Mater. Interfaces* **2020**, *12*, 12717–12726. [[CrossRef](#)]
54. Guchhait, A.; Dewi, H.A.; Leow, S.W.; Wang, H.; Han, G.; Suhaimi, F.B.; Mhaisalkar, S.; Wong, L.H.; Mathews, N. Over 20% efficient CIGS–perovskite tandem solar cells. *ACS Energy Lett.* **2017**, *2*, 807–812. [[CrossRef](#)]
55. Poncelet, O.; Kotipalli, R.; Vermang, B.; Macleod, A.; Francis, L.A.; Flandre, D. Optimisation of rear reflectance in ultra-thin CIGS solar cells towards > 20% efficiency. *Sol. Energy* **2017**, *146*, 443–452. [[CrossRef](#)]
56. Ma, P.; Li, W.; Yi, C.; Dai, C.; Luo, H.; Yang, C. Investigation of Mo films deposited on high temperature polyimide substrate by magnetron sputtering for flexible CIGS thin film solar cells application. *AIP Adv.* **2019**, *9*, 045024. [[CrossRef](#)]
57. Uličná, S.; Arnou, P.; Abbas, A.; Togay, M.; Welch, L.M.; Bliss, M.; Malkov, A.V.; Walls, J.M.; Bowers, J.W. Deposition and application of a Mo–N back contact diffusion barrier yielding a 12.0% efficiency solution-processed CIGS solar cell using an amine–thiol solvent system. *J. Mater. Chem. A* **2019**, *7*, 7042–7052. [[CrossRef](#)]
58. Jackson, P.; Wuerz, R.; Hariskos, D.; Lotter, E.; Witte, W.; Powalla, M. Effects of heavy alkali elements in Cu (In, Ga) Se<sub>2</sub> solar cells with efficiencies up to 22.6%. *Physica Status Solidi (RRL)–Rapid Res. Lett.* **2016**, *10*, 583–586. [[CrossRef](#)]
59. Li, H.; Chen, J.; Zhang, Y.; Wang, W.; Gu, H. Efficiency Enhancement of CIGS Solar Cells via Recombination Passivation. *ACS Appl. Energy Mater.* **2020**. [[CrossRef](#)]
60. Feurer, T.; Carron, R.; Torres Sevilla, G.; Fu, F.; Pisoni, S.; Romanyuk, Y.E.; Buecheler, S.; Tiwari, A.N. Efficiency Improvement of Near-Stoichiometric CuInSe<sub>2</sub> Solar Cells for Application in Tandem Devices. *Adv. Energy Mater.* **2019**, *9*, 1901428. [[CrossRef](#)]
61. Boubakeur, M.; Aissat, A.; Arbia, M.B.; Maaref, H.; Vilcot, J. Enhancement of the efficiency of ultra-thin CIGS/Si structure for solar cell applications. *Superlattices Microstruct.* **2020**, *138*, 106377. [[CrossRef](#)]
62. Hsueh, T.J.; Shieh, J.M.; Yeh, Y.M. Hybrid Cd-free CIGS solar cell/TEG device with ZnO nanowires. *Prog. Photovolt. Res. Appl.* **2015**, *23*, 507–512. [[CrossRef](#)]
63. Khatri, I.; Shudo, K.; Matsuura, J.; Sugiyama, M.; Nakada, T. Impact of heat-light soaking on potassium fluoride treated CIGS solar cells with CdS buffer layer. *Prog. Photovolt. Res. Appl.* **2018**, *26*, 171–178. [[CrossRef](#)]
64. Tobbeche, S.; Kalache, S.; Elbar, M.; Kateb, M.N.; Serdouk, M.R. Improvement of the CIGS solar cell performance: Structure based on a ZnS buffer layer. *Opt. Quantum Electron.* **2019**, *51*, 284. [[CrossRef](#)]
65. Rezaei, N.; Isabella, O.; Vroon, Z.; Zeman, M. Optical optimization of a multi-layer wideband anti-reflection coating using porous MgF<sub>2</sub> for sub-micron-thick CIGS solar cells. *Sol. Energy* **2019**, *177*, 59–67. [[CrossRef](#)]
66. Garud, S.; Gampa, N.; Allen, T.G.; Kotipalli, R.; Flandre, D.; Batuk, M.; Hadermann, J.; Meuris, M.; Poortmans, J.; Smets, A. Surface passivation of CIGS solar cells using gallium oxide. *Phys. Status Solidi* **2018**, *215*, 1700826. [[CrossRef](#)]
67. Qiao, S.; Liu, J.; Fu, G.; Ren, K.; Li, Z.; Wang, S.; Pan, C. ZnO nanowire based CIGS solar cell and its efficiency enhancement by the piezo-phototronic effect. *Nano Energy* **2018**, *49*, 508–514. [[CrossRef](#)]
68. Major, J.D.; Tena-Zaera, R.; Azaceta, E.; Bowen, L.; Durose, K. Development of ZnO nanowire based CdTe thin film solar cells. *Sol. Energy Mater. Sol. Cells* **2017**, *160*, 107–115. [[CrossRef](#)]
69. Li, Q.; Shen, K.; Yang, R.; Zhao, Y.; Lu, S.; Wang, R.; Dong, J.; Wang, D. Comparative study of GaAs and CdTe solar cell performance under low-intensity light irradiance. *Sol. Energy* **2017**, *157*, 216–226. [[CrossRef](#)]
70. Wang, T.; Zhu, X.; Li, W.; Zhang, J.; Wang, W. Incorporation of metal selenide thin films as the secondary absorber in the CdTe solar cells. *J. Alloy. Compd.* **2020**, *828*, 154415. [[CrossRef](#)]
71. Li, D.-B.; Bista, S.S.; Song, Z.; Awni, R.A.; Subedi, K.K.; Shrestha, N.; Pradhan, P.; Chen, L.; Bastola, E.; Grice, C.R. Maximize CdTe solar cell performance through copper activation engineering. *Nano Energy* **2020**, *73*, 104835. [[CrossRef](#)]
72. Zhao, J.; He, Y.; Tan, K.; Yang, J.; Chen, S.; Yuan, R. Novel ratiometric electrochemiluminescence biosensor based on BP-CdTe QDs with dual emission for detecting microRNA-126. *Anal. Chem.* **2021**, *93*, 12400–12408. [[CrossRef](#)]
73. Fang, Z.; Wang, X.C.; Wu, H.C.; Zhao, C.Z. Achievements and challenges of CdS/CdTe solar cells. *Int. J. Photoenergy* **2011**. [[CrossRef](#)]
74. Boudour, S.; Bouchama, I.; Bouarissa, N.; Hadjab, M. A study of CdTe solar cells using Ga-doped Mg<sub>x</sub>Zn<sub>1-x</sub>O buffer/TCO layers: Simulation and performance analysis. *J. Sci. Adv. Mater. Devices* **2019**, *4*, 111–115. [[CrossRef](#)]
75. Colegrove, E.; Banai, R.; Blissett, C.; Buurma, C.; Ellsworth, J.; Morley, M.; Barnes, S.; Gilmore, C.; Bergeson, J.; Dhere, R. High-efficiency polycrystalline CdS/CdTe solar cells on buffered commercial TCO-coated glass. *J. Electron. Mater.* **2012**, *41*, 2833–2837. [[CrossRef](#)]
76. Lv, B.; Yan, B.; Cai, P.; Gao, F.; Ye, Z.; Li, Y.; Chen, N.; Sui, C.; Lin, Q.; Cheng, G. The study on saturation current and ideality factor of CdTe solar cell based on CdS window layer deposited with hydrogen peroxide. *Semicond. Sci. Technol.* **2019**, *34*, 115025. [[CrossRef](#)]
77. He, X.; Wu, L.; Hao, X.; Zhang, J.; Li, C.; Wang, W.; Feng, L.; Du, Z. The Band Structures of Zn<sub>1-x</sub>Mg<sub>x</sub>O (In) and the Simulation of CdTe Solar Cells with a Zn<sub>1-x</sub>Mg<sub>x</sub>O (In) Window Layer by SCAPS. *Energies* **2019**, *12*, 291. [[CrossRef](#)]



78. Awni, R.A.; Li, D.B.; Song, Z.; Bista, S.S.; Razooqi, M.A.; Grice, C.R.; Chen, L.; Liyanage, G.K.; Li, C.; Phillips, A.B. Influences of buffer material and fabrication atmosphere on the electrical properties of CdTe solar cells. *Prog. Photovolt. Res. Appl.* **2019**, *27*, 1115–1123. [[CrossRef](#)]
79. Zhang, X.; Shen, S.; Howell, P.; Cheng, W.; Mubeen, S.; Stickney, J. Potential Pulse ALD for Room Temperature Fabrication of Stoichiometric CdTe Nanofilms. *J. Electrochem. Soc.* **2019**, *166*, H3249. [[CrossRef](#)]
80. Li, X.; Xiao, D.; Wu, L.; Wang, D.; Wang, G.; Wang, D. CdTe thin film solar cells with copper iodide as a back contact buffer layer. *Sol. Energy* **2019**, *185*, 324–332. [[CrossRef](#)]
81. Artegiani, E.; Menossi, D.; Shiel, H.; Dhanak, V.; Major, J.D.; Gasparotto, A.; Sun, K.; Romeo, A. Analysis of a novel CuCl<sub>2</sub> back contact process for improved stability in CdTe solar cells. *Prog. Photovolt. Res. Appl.* **2019**, *27*, 706–715.
82. Nagaoka, A.; Nishioka, K.; Yoshino, K.; Katsube, R.; Nose, Y.; Masuda, T.; Scarpulla, M.A. Comparison of Sb, As, and P doping in Cd-rich CdTe single crystals: Doping properties, persistent photoconductivity, and long-term stability. *Appl. Phys. Lett.* **2020**, *116*, 132102. [[CrossRef](#)]
83. Ojo, A.; Dharmadasa, I. 15.3% efficient graded bandgap solar cells fabricated using electroplated CdS and CdTe thin films. *Sol. Energy* **2016**, *136*, 10–14. [[CrossRef](#)]
84. Shen, K.; Yang, R.; Wang, D.; Jeng, M.; Chaudhary, S.; Ho, K.; Wang, D. Stable CdTe solar cell with V<sub>2</sub>O<sub>5</sub> as a back contact buffer layer. *Sol. Energy Mater. Sol. Cells* **2016**, *144*, 500–508. [[CrossRef](#)]
85. Yang, X.; Bao, Z.; Luo, R.; Liu, B.; Tang, P.; Li, B.; Zhang, J.; Li, W.; Wu, L.; Feng, L. Preparation and characterization of pulsed laser deposited CdS/CdSe bi-layer films for CdTe solar cell application. *Mater. Sci. Semicond. Process.* **2016**, *48*, 27–32. [[CrossRef](#)]
86. Hu, A.; Zhou, J.; Zhou, P.; Wu, X.; Yang, D. The role of O<sub>2</sub> in CdSeTe thin film deposition and CdSeTe/CdTe solar cell performance. *Sol. Energy Mater. Sol. Cells* **2020**, *214*, 110595. [[CrossRef](#)]
87. Shukla, V.; Panda, G. Numerical modelling of ultrathin CdTe solar cell with back surface field layer. In Proceedings of the IOP Conference Series: Materials Science and Engineering, Tamil Nadu, India, 9–10 April 2020; p. 012106.
88. Woods-Robinson, R.; Tursun Ablekim, A.N.; Johnston, S.; Persson, K.A.; Reese, M.O.; Metzger, W.K.; Zakutayev, A. Sputtered p-Type CuxZn<sub>1-x</sub>S Back Contact to CdTe Solar Cells. *ACS Appl. Energy Mater.* **2020**, *3*, 5427–5438. [[CrossRef](#)]
89. Parashar, D.; Krishna, V.G.; Moger, S.N.; Keshav, R.; Mahesha, M. Thickness Optimization of ZnO/CdS/CdTe Solar Cell by Numerical Simulation. *Trans. Electr. Electron. Mater.* **2020**, *21*, 587–593. [[CrossRef](#)]
90. Rehman, Q.; Khan, A.D.; Khan, A.D.; Noman, M.; Ali, H.; Rauf, A.; Ahmad, M.S. Super absorption of solar energy using a plasmonic nanoparticle based CdTe solar cell. *RSC Adv.* **2019**, *9*, 34207–34213. [[CrossRef](#)] [[PubMed](#)]
91. Paul, S.; Swartz, C.; Sohal, S.; Grice, C.; Bista, S.S.; Li, D.-B.; Yan, Y.; Holtz, M.; Li, J.V. Buffer/absorber interface recombination reduction and improvement of back-contact barrier height in CdTe solar cells. *Thin Solid Film.* **2019**, *685*, 385–392. [[CrossRef](#)]
92. Özen, Y. The enhancement in cell performance of CdTe-based solar cell with Si/SiO<sub>2</sub> distributed Bragg reflectors. *Appl. Phys. A* **2020**, *126*, 1–6. [[CrossRef](#)]
93. Omar, A.; Ali, M.S.; Abd Rahim, N. Electron transport properties analysis of titanium dioxide dye-sensitized solar cells (TiO<sub>2</sub>-DSSCs) based natural dyes using electrochemical impedance spectroscopy concept: A review. *Sol. Energy* **2020**, *207*, 1088–1121. [[CrossRef](#)]
94. Ikpesu, J.E.; Iyuke, S.E.; Daramola, M.; Okewale, A.O. Synthesis of improved dye-sensitized solar cell for renewable energy power generation. *Sol. Energy* **2020**, *206*, 918–934. [[CrossRef](#)]
95. Mehmood, U.; Asghar, H.; Babar, F.; Younas, M. Effect of graphene contents in polyaniline/graphene composites counter electrode material on the photovoltaic performance of dye-sensitized solar cells (DSSCs). *Sol. Energy* **2020**, *196*, 132–136. [[CrossRef](#)]
96. Mohamad, A.A. Physical properties of quasi-solid-state polymer electrolytes for dye-sensitized solar cells: A characterisation review. *Sol. Energy* **2019**, *190*, 434–452. [[CrossRef](#)]
97. Mahalingam, S.; Nugroho, A.; Floresyona, D.; Lau, K.S.; Manap, A.; Chia, C.H.; Afandi, N. Bio and non-bio materials-based quasi-solid state electrolytes in DSSC: A review. *Int. J. Energy Res.* **2022**, *46*, 5399–5422. [[CrossRef](#)]
98. Chowdhury, F.I.; Buraidah, M.; Arof, A.; Mellander, B.-E.; Noor, I. Impact of tetrabutylammonium, iodide and triiodide ions conductivity in polyacrylonitrile based electrolyte on DSSC performance. *Sol. Energy* **2020**, *196*, 379–388. [[CrossRef](#)]
99. Selvanathan, V.; Yahya, R.; Alharbi, H.F.; Alharthi, N.H.; Alharthi, Y.S.; Ruslan, M.H.; Amin, N.; Akhtaruzzaman, M. Organosoluble starch derivative as quasi-solid electrolytes in DSSC: Unravelling the synergy between electrolyte rheology and photovoltaic properties. *Sol. Energy* **2020**, *197*, 144–153. [[CrossRef](#)]
100. Subalakshmi, K.; Kumar, K.A.; Paul, O.P.; Saraswathy, S.; Pandurangan, A.; Senthilselvan, J. Platinum-free metal sulfide counter electrodes for DSSC applications: Structural, electrochemical and power conversion efficiency analyses. *Sol. Energy* **2019**, *193*, 507–518. [[CrossRef](#)]
101. Roy, A.; Ghosh, A.; Bhandari, S.; Selvaraj, P.; Sundaram, S.; Mallick, T.K. Color comfort evaluation of dye-sensitized solar cell (DSSC) based building-integrated photovoltaic (BIPV) glazing after 2 years of ambient exposure. *J. Phys. Chem. C* **2019**, *123*, 23834–23837. [[CrossRef](#)]
102. Ahmad, M.S.; Pandey, A.K.; Abd Rahim, N. Advancements in the development of TiO<sub>2</sub> photoanodes and its fabrication methods for dye sensitized solar cell (DSSC) applications. A review. *Renew. Sustain. Energy Rev.* **2017**, *77*, 89–108. [[CrossRef](#)]
103. Syafinar, R.; Gomesh, N.; Irwanto, M.; Fareq, M.; Irwan, Y. Chlorophyll pigments as nature based dye for dye-sensitized solar cell (DSSC). *Energy Procedia* **2015**, *79*, 896–902. [[CrossRef](#)]

104. Ayalew, W.A.; Ayele, D.W. Dye-sensitized solar cells using natural dye as light-harvesting materials extracted from *Acanthus sennii* chiovenda flower and *Euphorbia cotinifolia* leaf. *J. Sci. Adv. Mater. Devices* **2016**, *1*, 488–494. [[CrossRef](#)]
105. Murugadoss, V.; Panneerselvam, P.; Yan, C.; Guo, Z.; Angaiah, S. A simple one-step hydrothermal synthesis of cobaltnickel selenide/graphene nanohybrid as an advanced platinum free counter electrode for dye sensitized solar cell. *Electrochim. Acta* **2019**, *312*, 157–167. [[CrossRef](#)]
106. Kumarasinghe, K.; Kumara, G.; Rajapakse, R.; Liyanage, D.; Tennakone, K. Activated coconut shell charcoal based counter electrode for dye-sensitized solar cells. *Org. Electron.* **2019**, *71*, 93–97. [[CrossRef](#)]
107. Calogero, G.; Yum, J.-H.; Sinopoli, A.; Di Marco, G.; Grätzel, M.; Nazeeruddin, M.K. Anthocyanins and betalains as light-harvesting pigments for dye-sensitized solar cells. *Sol. Energy* **2012**, *86*, 1563–1575. [[CrossRef](#)]
108. Wu, X.; Duan, J.; Zhao, Y.; Yang, X.; Chen, H.; He, B.; Tang, Q. Co/Se and Ni/Se nanocomposite films prepared by magnetron sputtering as counter electrodes for dye-sensitized solar cells. *Sol. Energy* **2019**, *180*, 85–91. [[CrossRef](#)]
109. Lai, W.H.; Su, Y.H.; Teoh, L.G.; Hon, M.H. Commercial and natural dyes as photosensitizers for a water-based dye-sensitized solar cell loaded with gold nanoparticles. *J. Photochem. Photobiol. A Chem.* **2008**, *195*, 307–313. [[CrossRef](#)]
110. Kohn, S.; Großhede, C.; Storck, J.L.; Grötsch, G.; Cornelißen, C.; Streitenberger, A.; Grassmann, C.; Schwarz-Pfeiffer, A.; Ehrmann, A. Commercially available teas as possible dyes for dye-sensitized solar cells. *Optik* **2019**, *185*, 178–182. [[CrossRef](#)]
111. Kang, H.-Y.; Wang, H.P. Cu@ C dispersed TiO<sub>2</sub> for dye-sensitized solar cell photoanodes. *Appl. Energy* **2012**, *100*, 144–147. [[CrossRef](#)]
112. Kabir, F.; Bhuiyan, M.; Manir, M.; Rahaman, M.; Khan, M.; Ikegami, T. Development of dye-sensitized solar cell based on combination of natural dyes extracted from Malabar spinach and red spinach. *Results Phys.* **2019**, *14*, 102474. [[CrossRef](#)]
113. Mohammed, I.K.; Uthman, I.K.; Muhammad, M.N. Photoelectric characterization of dye sensitized solar cells using natural dye from pawpaw leaf and flame tree flower as sensitizers. *Physics* **2012**, *3*, 281–286.
114. Babkair, S.S.; Alzubaydi, R.A.; Ansari, A.A.; Al-Hadeethi, Y. Dye sensitized solar cells based on double-layered titanium dioxide and their evaluation in tropical hot desert climate of Saudi Arabia. *Superlattices Microstruct.* **2019**, *133*, 106206. [[CrossRef](#)]
115. Maurya, I.C.; Srivastava, P.; Bahadur, L. Dye-sensitized solar cell using extract from petals of male flowers *Luffa cylindrica* L. as a natural sensitizer. *Opt. Mater.* **2016**, *52*, 150–156. [[CrossRef](#)]
116. Chang, H.; Wu, H.; Chen, T.; Huang, K.; Jwo, C.; Lo, Y. Dye-sensitized solar cell using natural dyes extracted from spinach and ipomoea. *J. Alloy. Compd.* **2010**, *495*, 606–610. [[CrossRef](#)]
117. Gómez-Ortíz, N.; Vázquez-Maldonado, I.; Pérez-Espadas, A.; Mena-Rejón, G.; Azamar-Barrios, J.; Oskam, G. Dye-sensitized solar cells with natural dyes extracted from achiote seeds. *Sol. Energy Mater. Sol. Cells* **2010**, *94*, 40–44. [[CrossRef](#)]
118. Park, N.-G. Perovskite solar cells: An emerging photovoltaic technology. *Mater. Today* **2015**, *18*, 65–72. [[CrossRef](#)]
119. Petrus, M.L.; Schlipf, J.; Li, C.; Gujar, T.P.; Giesbrecht, N.; Müller-Buschbaum, P.; Thelakkat, M.; Bein, T.; Hüttner, S.; Docampo, P. Capturing the sun: A review of the challenges and perspectives of perovskite solar cells. *Adv. Energy Mater.* **2017**, *7*, 1700264. [[CrossRef](#)]
120. Li, Z.; Klein, T.R.; Kim, D.H.; Yang, M.; Berry, J.J.; van Hest, M.F.; Zhu, K. Scalable fabrication of perovskite solar cells. *Nat. Rev. Mater.* **2018**, *3*, 1–20. [[CrossRef](#)]
121. Qiao, H.W.; Yang, S.; Wang, Y.; Chen, X.; Wen, T.Y.; Tang, L.J.; Cheng, Q.; Hou, Y.; Zhao, H.; Yang, H.G. A Gradient Heterostructure Based on Tolerance Factor in High-Performance Perovskite Solar Cells with 0.84 Fill Factor. *Adv. Mater.* **2019**, *31*, 1804217. [[CrossRef](#)]
122. Chen, S.; Dai, X.; Xu, S.; Jiao, H.; Zhao, L.; Huang, J. Stabilizing perovskite-substrate interfaces for high-performance perovskite modules. *Science* **2021**, *373*, 902–907. [[CrossRef](#)]
123. Yin, W.-J.; Yang, J.-H.; Kang, J.; Yan, Y.; Wei, S.-H. Halide perovskite materials for solar cells: A theoretical review. *J. Mater. Chem. A* **2015**, *3*, 8926–8942. [[CrossRef](#)]
124. Song, Z.; Wathage, S.C.; Phillips, A.B.; Heben, M.J. Pathways toward high-performance perovskite solar cells: Review of recent advances in organo-metal halide perovskites for photovoltaic applications. *J. Photonics Energy* **2016**, *6*, 022001. [[CrossRef](#)]
125. Dey, A.; Ye, J.; De, A.; Debroye, E.; Ha, S.K.; Bladt, E.; Kshirsagar, A.S.; Wang, Z.; Yin, J.; Wang, Y. State of the art and prospects for halide perovskite nanocrystals. *ACS Nano* **2021**, *15*, 10775–10981. [[CrossRef](#)]
126. Madhavan, V.E.; Zimmermann, I.; Roldán-Carmona, C.; Grancini, G.; Buffiere, M.; Belaidi, A.; Nazeeruddin, M.K. Copper thiocyanate inorganic hole-transporting material for high-efficiency perovskite solar cells. *ACS Energy Lett.* **2016**, *1*, 1112–1117. [[CrossRef](#)]
127. Bakr, Z.H.; Wali, Q.; Fakharuddin, A.; Schmidt-Mende, L.; Brown, T.M.; Jose, R. Advances in hole transport materials engineering for stable and efficient perovskite solar cells. *Nano Energy* **2017**, *34*, 271–305. [[CrossRef](#)]
128. Salado, M.; Oliva-Ramirez, M.; Kazim, S.; González-Elipse, A.R.; Ahmad, S. 1-dimensional TiO<sub>2</sub> nano-forests as photoanodes for efficient and stable perovskite solar cells fabrication. *Nano Energy* **2017**, *35*, 215–222. [[CrossRef](#)]
129. Wang, Z.; Shi, Z.; Li, T.; Chen, Y.; Huang, W. Stability of perovskite solar cells: A prospective on the substitution of the A cation and X anion. *Angew. Chem. Int. Ed.* **2017**, *56*, 1190–1212. [[CrossRef](#)] [[PubMed](#)]
130. Wang, D.; Wright, M.; Elumalai, N.K.; Uddin, A. Stability of perovskite solar cells. *Sol. Energy Mater. Sol. Cells* **2016**, *147*, 255–275. [[CrossRef](#)]
131. Bouich, A.; Marí-Guaita, J.; Soucase, B.M.; Palacios, P. Manufacture of high-efficiency and stable lead-free solar cells through antisolvent quenching engineering. *Nanomaterials* **2022**, *12*, 2901. [[CrossRef](#)]

132. Freitas, J.N.; Gonçalves, A.S.; Nogueira, A.F. A comprehensive review of the application of chalcogenide nanoparticles in polymer solar cells. *Nanoscale* **2014**, *6*, 6371–6397. [[CrossRef](#)]
133. Hau, S.K.; Yip, H.-L.; Jen, A.K.-Y. A review on the development of the inverted polymer solar cell architecture. *Polym. Rev.* **2010**, *50*, 474–510. [[CrossRef](#)]
134. Mei, A.; Li, X.; Liu, L.; Ku, Z.; Liu, T.; Rong, Y.; Xu, M.; Hu, M.; Chen, J.; Yang, Y. A hole-conductor-free, fully printable mesoscopic perovskite solar cell with high stability. *Science* **2014**, *345*, 295–298. [[CrossRef](#)]
135. Chen, H.; Wei, Z.; Zheng, X.; Yang, S. A scalable electrodeposition route to the low-cost, versatile and controllable fabrication of perovskite solar cells. *Nano Energy* **2015**, *15*, 216–226. [[CrossRef](#)]
136. Seo, J.; Park, S.; Kim, Y.C.; Jeon, N.J.; Noh, J.H.; Yoon, S.C.; Seok, S.I. Benefits of very thin PCBM and LiF layers for solution-processed p–i–n perovskite solar cells. *Energy Environ. Sci.* **2014**, *7*, 2642–2646. [[CrossRef](#)]
137. Tang, S.; Deng, Y.; Zheng, X.; Bai, Y.; Fang, Y.; Dong, Q.; Wei, H.; Huang, J. Composition engineering in doctor-blading of perovskite solar cells. *Adv. Energy Mater.* **2017**, *7*, 1700302. [[CrossRef](#)]
138. Chang, W.C.; Lan, D.H.; Lee, K.M.; Wang, X.F.; Liu, C.L. Controlled deposition and performance optimization of perovskite solar cells using ultrasonic spray-coating of photoactive layers. *ChemSusChem* **2017**, *10*, 1405–1412. [[CrossRef](#)] [[PubMed](#)]
139. Huang, L.; Li, C.; Sun, X.; Xu, R.; Du, Y.; Ni, J.; Cai, H.; Li, J.; Hu, Z.; Zhang, J. Efficient and hysteresis-less pseudo-planar heterojunction perovskite solar cells fabricated by a facile and solution-saving one-step dip-coating method. *Org. Electron.* **2017**, *40*, 13–23. [[CrossRef](#)]
140. Lee, J.-W.; Na, S.-I.; Kim, S.-S. Efficient spin-coating-free planar heterojunction perovskite solar cells fabricated with successive brush-painting. *J. Power Sources* **2017**, *339*, 33–40. [[CrossRef](#)]
141. Liao, H.C.; Guo, P.; Hsu, C.P.; Lin, M.; Wang, B.; Zeng, L.; Huang, W.; Soe, C.M.M.; Su, W.F.; Bedzyk, M.J. Enhanced efficiency of hot-cast large-area planar perovskite solar cells/modules having controlled chloride incorporation. *Adv. Energy Mater.* **2017**, *7*, 1601660. [[CrossRef](#)]
142. Ku, Z.; Rong, Y.; Xu, M.; Liu, T.; Han, H. Full printable processed mesoscopic CH<sub>3</sub> NH<sub>3</sub> PbI<sub>3</sub>/TiO<sub>2</sub> heterojunction solar cells with carbon counter electrode. *Sci. Rep.* **2013**, *3*, 3132. [[CrossRef](#)]
143. Leyden, M.R.; Lee, M.V.; Raga, S.R.; Qi, Y. Large formamidinium lead trihalide perovskite solar cells using chemical vapor deposition with high reproducibility and tunable chlorine concentrations. *J. Mater. Chem. A* **2015**, *3*, 16097–16103. [[CrossRef](#)]
144. Gao, L.-L.; Li, C.-X.; Li, C.-J.; Yang, G.-J. Large-area high-efficiency perovskite solar cells based on perovskite films dried by the multi-flow air knife method in air. *J. Mater. Chem. A* **2017**, *5*, 1548–1557. [[CrossRef](#)]
145. He, M.; Li, B.; Cui, X.; Jiang, B.; He, Y.; Chen, Y.; O’Neil, D.; Szymanski, P.; Ei-Sayed, M.A.; Huang, J. Meniscus-assisted solution printing of large-grained perovskite films for high-efficiency solar cells. *Nat. Commun.* **2017**, *8*, 1–10. [[CrossRef](#)]
146. Krebs, F.C. Fabrication and processing of polymer solar cells: A review of printing and coating techniques. *Sol. Energy Mater. Sol. Cells* **2009**, *93*, 394–412. [[CrossRef](#)]
147. Po, R.; Carbonera, C.; Bernardi, A.; Tinti, F.; Camaioni, N. Polymer-and carbon-based electrodes for polymer solar cells: Toward low-cost, continuous fabrication over large area. *Sol. Energy Mater. Sol. Cells* **2012**, *100*, 97–114. [[CrossRef](#)]
148. Cai, W.; Gong, X.; Cao, Y. Polymer solar cells: Recent development and possible routes for improvement in the performance. *Sol. Energy Mater. Sol. Cells* **2010**, *94*, 114–127. [[CrossRef](#)]
149. Wang, Q.; Xie, Y.; Soltani-Kordshuli, F.; Eslamian, M. Progress in emerging solution-processed thin film solar cells—Part I: Polymer solar cells. *Renew. Sustain. Energy Rev.* **2016**, *56*, 347–361. [[CrossRef](#)]
150. Lu, L.; Zheng, T.; Wu, Q.; Schneider, A.M.; Zhao, D.; Yu, L. Recent advances in bulk heterojunction polymer solar cells. *Chem. Rev.* **2015**, *115*, 12666–12731. [[CrossRef](#)]
151. You, J.; Dou, L.; Hong, Z.; Li, G.; Yang, Y. Recent trends in polymer tandem solar cells research. *Prog. Polym. Sci.* **2013**, *38*, 1909–1928. [[CrossRef](#)]
152. Jhuo, H.J.; Yeh, P.N.; Liao, S.H.; Li, Y.L.; Cheng, Y.S.; Chen, S.A. Review on the recent progress in low band gap conjugated polymers for bulk hetero-junction polymer solar cells. *J. Chin. Chem. Soc.* **2014**, *61*, 115–126. [[CrossRef](#)]
153. Xu, X.; Feng, K.; Bi, Z.; Ma, W.; Zhang, G.; Peng, Q. Single-junction polymer solar cells with 16.35% efficiency enabled by a platinum (II) complexation strategy. *Adv. Mater.* **2019**, *31*, 1901872. [[CrossRef](#)] [[PubMed](#)]
154. Mohapatra, A.; Singh, A.; Abbas, S.A.; Lu, Y.-J.; Boopathi, K.M.; Hanmandlu, C.; Kaisar, N.; Lee, C.-H.; Chu, C.-W. Bilayer polymer solar cells prepared with transfer printing of active layers from controlled swelling/de-swelling of PDMS. *Nano Energy* **2019**, *63*, 103826. [[CrossRef](#)]
155. Huang, L.; Jiang, P.; Zhang, Y.; Zhang, L.; Yu, Z.; He, Q.; Zhou, W.; Tan, L.; Chen, Y. Unraveling the Morphology in Solution-Processed Pseudo-Bilayer Planar Heterojunction Organic Solar Cells. *ACS Appl. Mater. Interfaces* **2019**, *11*, 26213–26221. [[CrossRef](#)]
156. St. Onge, P.B.J.; Ocheje, M.U.; Selivanova, M.; Rondeau-Gagne, S. Recent advances in mechanically robust and stretchable bulk heterojunction polymer solar cells. *Chem. Rec.* **2019**, *19*, 1008–1027. [[CrossRef](#)]
157. Lee, S.J.; Kim, S.; Lim, D.C.; Kim, D.H.; Nahm, S.; Han, S.H. Inverted bulk-heterojunction polymer solar cells using a sputter-deposited Al-doped ZnO electron transport layer. *J. Alloy. Compd.* **2019**, *777*, 717–722. [[CrossRef](#)]
158. Li, Q.; Wang, L.-M.; Liu, S.; Zhan, X.; Zhu, T.; Cao, Z.; Lai, H.; Zhao, J.; Cai, Y.; Xie, W. Impact of Donor–Acceptor Interaction and Solvent Additive on the Vertical Composition Distribution of Bulk Heterojunction Polymer Solar Cells. *ACS Appl. Mater. Interfaces* **2019**, *11*, 45979–45990. [[CrossRef](#)] [[PubMed](#)]



159. Xu, Y.; Yuan, J.; Liang, S.; Chen, J.-D.; Xia, Y.; Larson, B.W.; Wang, Y.; Su, G.M.; Zhang, Y.; Cui, C. Simultaneously improved efficiency and stability in all-polymer solar cells by a P–i–N architecture. *ACS Energy Lett.* **2019**, *4*, 2277–2286. [[CrossRef](#)]
160. Kim, M.; Kim, H.I.; Ryu, S.U.; Son, S.Y.; Park, S.A.; Khan, N.; Shin, W.S.; Song, C.E.; Park, T. Improving the Photovoltaic Performance and Mechanical Stability of Flexible All-Polymer Solar Cells via Tailoring Intermolecular Interactions. *Chem. Mater.* **2019**, *31*, 5047–5055. [[CrossRef](#)]
161. Zhao, R.; Wang, N.; Yu, Y.; Liu, J. Organoboron polymer for 10% efficiency all-polymer solar cells. *Chem. Mater.* **2020**, *32*, 1308–1314. [[CrossRef](#)]
162. Sun, C.; Qin, S.; Wang, R.; Chen, S.; Pan, F.; Qiu, B.; Shang, Z.; Meng, L.; Zhang, C.; Xiao, M. High efficiency polymer solar cells with efficient hole transfer at zero highest occupied molecular orbital offset between methylated polymer donor and brominated acceptor. *J. Am. Chem. Soc.* **2020**, *142*, 1465–1474. [[CrossRef](#)]
163. Hu, Z.; Wang, Z.; An, Q.; Zhang, F. Semitransparent polymer solar cells with 12.37% efficiency and 18.6% average visible transmittance. *Sci. Bull.* **2020**, *65*, 131–137. [[CrossRef](#)]
164. An, Q.; Wang, J.; Gao, W.; Ma, X.; Hu, Z.; Gao, J.; Xu, C.; Hao, M.; Zhang, X.; Yang, C. Alloy-like ternary polymer solar cells with over 17.2% efficiency. *Sci. Bull.* **2020**, *65*, 538–545. [[CrossRef](#)]
165. Wu, Y.; Zheng, Y.; Yang, H.; Sun, C.; Dong, Y.; Cui, C.; Yan, H.; Li, Y. Rationally pairing photoactive materials for high-performance polymer solar cells with efficiency of 16.53%. *Sci. China Chem.* **2020**, *63*, 265–271. [[CrossRef](#)]
166. Ma, Y.; Zhou, X.; Cai, D.; Tu, Q.; Ma, W.; Zheng, Q. A minimal benzo [c][1, 2, 5] thiazazole-based electron acceptor as a third component material for ternary polymer solar cells with efficiencies exceeding 16.0%. *Mater. Horiz.* **2020**, *7*, 117–124. [[CrossRef](#)]
167. Yao, H.; Ma, L.K.; Yu, H.; Yu, J.; Chow, P.C.; Xue, W.; Zou, X.; Chen, Y.; Liang, J.; Arunagiri, L. All-Polymer Solar Cells with over 12% Efficiency and a Small Voltage Loss Enabled by a Polymer Acceptor Based on an Extended Fused Ring Core. *Adv. Energy Mater.* **2020**, *10*, 2001408. [[CrossRef](#)]
168. Yao, C.; Zhao, J.; Zhu, Y.; Liu, B.; Yan, C.; Perepichka, D.F.; Meng, H. Trifluoromethyl Group-Modified Non-Fullerene Acceptor toward Improved Power Conversion Efficiency over 13% in Polymer Solar Cells. *ACS Appl. Mater. Interfaces* **2020**, *12*, 11543–11550. [[CrossRef](#)] [[PubMed](#)]
169. An, Q.; Ma, X.; Gao, J.; Zhang, F. Solvent additive-free ternary polymer solar cells with 16.27% efficiency. *Sci. Bull.* **2019**, *64*, 504–506. [[CrossRef](#)]
170. Yao, H.; Bai, F.; Hu, H.; Arunagiri, L.; Zhang, J.; Chen, Y.; Yu, H.; Chen, S.; Liu, T.; Lai, J.Y.L. Efficient all-polymer solar cells based on a new polymer acceptor achieving 10.3% power conversion efficiency. *ACS Energy Lett.* **2019**, *4*, 417–422. [[CrossRef](#)]
171. Meng, Y.; Wu, J.; Guo, X.; Su, W.; Zhu, L.; Fang, J.; Zhang, Z.-G.; Liu, F.; Zhang, M.; Russell, T.P. 11.2% Efficiency all-polymer solar cells with high open-circuit voltage. *Sci. China Chem.* **2019**, *62*, 845–850. [[CrossRef](#)]
172. Nozik, A.J. Quantum dot solar cells. *Phys. E: Low-Dimens. Syst. Nanostructures* **2002**, *14*, 115–120. [[CrossRef](#)]
173. Kamat, P.V. Quantum dot solar cells. Semiconductor nanocrystals as light harvesters. *J. Phys. Chem. C* **2008**, *112*, 18737–18753. [[CrossRef](#)]
174. Liu, J.; Xian, K.; Ye, L.; Zhou, Z. Open-Circuit Voltage Loss in Lead Chalcogenide Quantum Dot Solar Cells. *Adv. Mater.* **2021**, *33*, 2008115. [[CrossRef](#)]
175. Chen, J.; Jia, D.; Johansson, E.M.; Hagfeldt, A.; Zhang, X. Emerging perovskite quantum dot solar cells: Feasible approaches to boost performance. *Energy Environ. Sci.* **2021**, *14*, 224–261. [[CrossRef](#)]
176. Albaladejo-Siguan, M.; Baird, E.C.; Becker-Koch, D.; Li, Y.; Rogach, A.L.; Vaynzof, Y. Stability of quantum dot solar cells: A matter of (Life) Time. *Adv. Energy Mater.* **2021**, *11*, 2003457. [[CrossRef](#)]
177. Nozik, A.J.; Beard, M.C.; Luther, J.M.; Law, M.; Ellingson, R.J.; Johnson, J.C. Semiconductor quantum dots and quantum dot arrays and applications of multiple exciton generation to third-generation photovoltaic solar cells. *Chem. Rev.* **2010**, *110*, 6873–6890. [[CrossRef](#)] [[PubMed](#)]
178. Kramer, I.J.; Sargent, E.H. Colloidal quantum dot photovoltaics: A path forward. *ACS Nano* **2011**, *5*, 8506–8514. [[CrossRef](#)] [[PubMed](#)]
179. Ip, A.H.; Thon, S.M.; Hoogland, S.; Voznyy, O.; Zhitomirsky, D.; Debnath, R.; Levina, L.; Rollny, L.R.; Carey, G.H.; Fischer, A. Hybrid passivated colloidal quantum dot solids. *Nat. Nanotechnol.* **2012**, *7*, 577–582. [[CrossRef](#)] [[PubMed](#)]
180. Yella, A.; Lee, H.-W.; Tsao, H.N.; Yi, C.; Chandiran, A.K.; Nazeeruddin, M.K.; Diau, E.W.-G.; Yeh, C.-Y.; Zakeeruddin, S.M.; Grätzel, M. Porphyrin-sensitized solar cells with cobalt (II/III)-based redox electrolyte exceed 12 percent efficiency. *Science* **2011**, *334*, 629–634. [[CrossRef](#)] [[PubMed](#)]
181. Lee, M.M.; Teuscher, J.; Miyasaka, T.; Murakami, T.N.; Snaith, H.J. Efficient hybrid solar cells based on meso-superstructured organometal halide perovskites. *Science* **2012**, *338*, 643–647. [[CrossRef](#)] [[PubMed](#)]
182. Brown, P.; Kamat, P.V. Quantum dot solar cells. electrophoretic deposition of CdSe– C60 composite films and capture of photogenerated electrons with n C60 cluster shell. *J. Am. Chem. Soc.* **2008**, *130*, 8890–8891. [[CrossRef](#)]
183. Park, J.; Kirch, J.; Mawst, L.; Liu, C.-C.; Nealey, P.; Kuech, T. Controlled growth of InGaAs/InGaAsP quantum dots on InP substrates employing diblock copolymer lithography. *Appl. Phys. Lett.* **2009**, *95*, 113111. [[CrossRef](#)]
184. Palankar, R.; Medvedev, N.; Rong, A.; Delcea, M. Fabrication of quantum dot microarrays using electron beam lithography for applications in analyte sensing and cellular dynamics. *ACS Nano* **2013**, *7*, 4617–4628. [[CrossRef](#)]
185. Di, D.; Perez-Wurfl, I.; Gentle, A.; Kim, D.-H.; Hao, X.; Shi, L.; Conibeer, G.; Green, M.A. Impacts of post-metallisation processes on the electrical and photovoltaic properties of Si quantum dot solar cells. *Nanoscale Res. Lett.* **2010**, *5*, 1762. [[CrossRef](#)]

186. Verma, V.B.; Stevens, M.J.; Silverman, K.L.; Dias, N.; Garg, A.; Coleman, J.J.; Mirin, R.P. Time-resolved photoluminescence of lithographically defined quantum dots fabricated by electron beam lithography and wet chemical etching. *J. Appl. Phys.* **2011**, *109*, 123112. [[CrossRef](#)]
187. Koguchi, N.; Ishige, K.; Takahashi, S. New selective molecular-beam epitaxial growth method for direct formation of GaAs quantum dots. *J. Vac. Sci. Technol. B Microelectron. Nanometer Struct. Process. Meas. Phenom.* **1993**, *11*, 787–790. [[CrossRef](#)]
188. Watanabe, K.; Koguchi, N.; Gotoh, Y. Fabrication of GaAs quantum dots by modified droplet epitaxy. *Jpn. J. Appl. Phys.* **2000**, *39*, L79. [[CrossRef](#)]
189. Leonard, D.; Krishnamurthy, M.; Fafard, S.; Merz, J.; Petroff, P. Molecular-beam epitaxy growth of quantum dots from strained coherent uniform islands of InGaAs on GaAs. *J. Vac. Sci. Technol. B Microelectron. Nanometer Struct. Process. Meas. Phenom.* **1994**, *12*, 1063–1066. [[CrossRef](#)]
190. Nose, K.; Omata, T.; Otsuka-Yao-Matsuo, S. Colloidal synthesis of ternary copper indium diselenide quantum dots and their optical properties. *J. Phys. Chem. C* **2009**, *113*, 3455–3460. [[CrossRef](#)]
191. Pu, Y.; Cai, F.; Wang, D.; Wang, J.-X.; Chen, J.-F. Colloidal synthesis of semiconductor quantum dots toward large-scale production: A review. *Ind. Eng. Chem. Res.* **2018**, *57*, 1790–1802. [[CrossRef](#)]
192. Rajh, T.; Micic, O.I.; Nozik, A.J. Synthesis and characterization of surface-modified colloidal cadmium telluride quantum dots. *J. Phys. Chem.* **1993**, *97*, 11999–12003. [[CrossRef](#)]
193. Lv, M.; Zhu, J.; Huang, Y.; Li, Y.; Shao, Z.; Xu, Y.; Dai, S. Colloidal CuInS<sub>2</sub> quantum dots as inorganic hole-transporting material in perovskite solar cells. *ACS Appl. Mater. Interfaces* **2015**, *7*, 17482–17488. [[CrossRef](#)]
194. Diguna, L.J.; Shen, Q.; Kobayashi, J.; Toyoda, T. High efficiency of CdSe quantum-dot-sensitized TiO<sub>2</sub> inverse opal solar cells. *Appl. Phys. Lett.* **2007**, *91*, 023116. [[CrossRef](#)]
195. Luo, J.; Wei, H.; Huang, Q.; Hu, X.; Zhao, H.; Yu, R.; Li, D.; Luo, Y.; Meng, Q. Highly efficient core-shell CuInS<sub>2</sub>-Mn doped CdS quantum dot sensitized solar cells. *Chem. Commun.* **2013**, *49*, 3881–3883. [[CrossRef](#)]
196. Zhao, K.; Pan, Z.; Mora-Seró, I.n.; Cánovas, E.; Wang, H.; Song, Y.; Gong, X.; Wang, J.; Bonn, M.; Bisquert, J. Boosting power conversion efficiencies of quantum-dot-sensitized solar cells beyond 8% by recombination control. *J. Am. Chem. Soc.* **2015**, *137*, 5602–5609. [[CrossRef](#)]
197. Ren, Z.; Wang, Z.; Wang, R.; Pan, Z.; Gong, X.; Zhong, X. Effects of metal oxyhydroxide coatings on photoanode in quantum dot sensitized solar cells. *Chem. Mater.* **2016**, *28*, 2323–2330. [[CrossRef](#)]
198. González-Pedro, V.; Sima, C.; Marzari, G.; Boix, P.P.; Giménez, S.; Shen, Q.; Dittrich, T.; Mora-Seró, I. High performance PbS Quantum Dot Sensitized Solar Cells exceeding 4% efficiency: The role of metal precursors in the electron injection and charge separation. *Phys. Chem. Chem. Phys.* **2013**, *15*, 13835–13843. [[CrossRef](#)]
199. Pan, Z.; Mora-Seró, I.n.; Shen, Q.; Zhang, H.; Li, Y.; Zhao, K.; Wang, J.; Zhong, X.; Bisquert, J. High-efficiency “green” quantum dot solar cells. *J. Am. Chem. Soc.* **2014**, *136*, 9203–9210. [[CrossRef](#)] [[PubMed](#)]
200. Jiao, S.; Shen, Q.; Mora-Seró, I.; Wang, J.; Pan, Z.; Zhao, K.; Kuga, Y.; Zhong, X.; Bisquert, J. Band engineering in core/shell ZnTe/CdSe for photovoltage and efficiency enhancement in exciplex quantum dot sensitized solar cells. *ACS Nano* **2015**, *9*, 908–915. [[CrossRef](#)] [[PubMed](#)]
201. Kim, S.; Kang, M.; Kim, S.; Heo, J.-H.; Noh, J.H.; Im, S.H.; Seok, S.I.; Kim, S.-W. Fabrication of CuInTe<sub>2</sub> and CuInTe<sub>2-x</sub>Se<sub>x</sub> Ternary Gradient Quantum Dots and Their Application to Solar Cells. *ACS Nano* **2013**, *7*, 4756–4763. [[CrossRef](#)] [[PubMed](#)]
202. Zhang, Q.; Guo, X.; Huang, X.; Huang, S.; Li, D.; Luo, Y.; Shen, Q.; Toyoda, T.; Meng, Q. Highly efficient CdS/CdSe-sensitized solar cells controlled by the structural properties of compact porous TiO<sub>2</sub> photoelectrodes. *Phys. Chem. Chem. Phys.* **2011**, *13*, 4659–4667. [[CrossRef](#)]
203. Yang, X.; Wang, K.; Gu, Y.; Ni, H.; Wang, X.; Yang, T.; Wang, Z. Improved efficiency of InAs/GaAs quantum dots solar cells by Si-doping. *Sol. Energy Mater. Sol. Cells* **2013**, *113*, 144–147. [[CrossRef](#)]